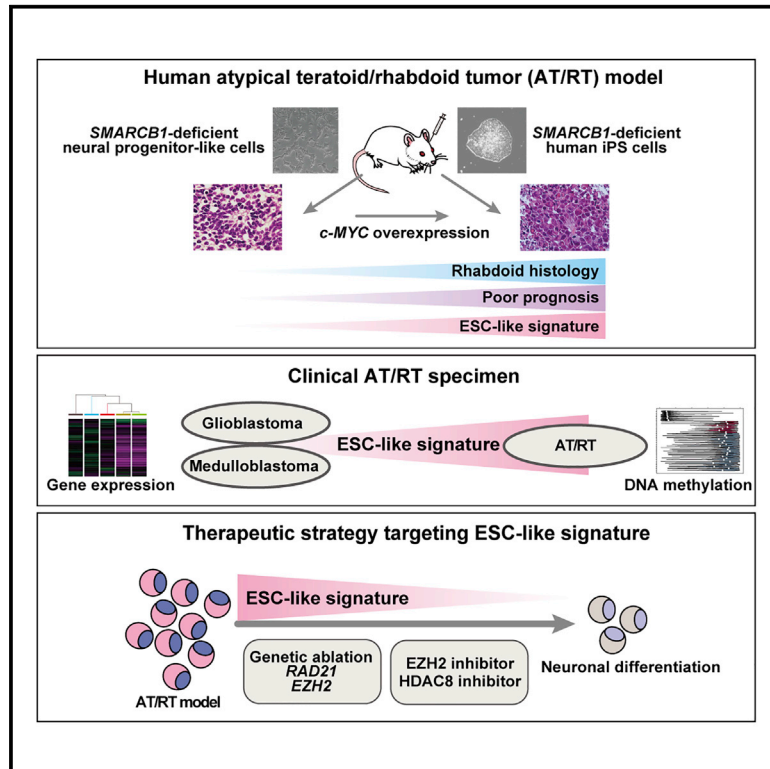# Human Pluripotent Stem Cell-Derived Tumor Model Uncovers the Embryonic Stem Cell Signature as a Key Driver in Atypical Teratoid/Rhabdoid Tumor

Graphical Abstract

Authors

Yukinori Terada, Norihide Jo, Yoshiki Arakawa, ..., Susumu Miyamoto, Takuya Yamamoto, Yasuhiro Yamada

Correspondence

yasu@ims.u-tokyo.ac.jp

In Brief

Terada et al. present *SMARCB1*-deficient human pluripotent stem cell-derived atypical teratoid/rhabdoid tumor (AT/RT) models and show that ESC-like signature is a critical driver of malignant phenotypes of AT/RT. Genetic ablation targeting the maintenance of pluripotency inhibits AT/RT cell growth, suggesting that the ESC-like signature could be a promising therapeutic target for AT/RT.

Highlights

- *SMARCB1*-deficient human iPSCs give rise to AT/RT-like tumors

- ESC-like signature induces rhabdoid histology and causes a poor prognosis

- AT/RT exhibits ESC-like transcriptional signature and DNA methylation landscape

- ESC-like signature could be a therapeutic target for AT/RT

CellPress

Human Pluripotent Stem Cell-Derived Tumor Model Uncovers the Embryonic Stem Cell Signature as a Key Driver in Atypical Teratoid/Rhabdoid Tumor

Yukinori Terada,[1,2,3,6] Norihide Jo,[2,6] Yoshiki Arakawa,[3] Megumi Sakakura,[1,2] Yosuke Yamada,[2] Tomoyo Ukai,[1,2] Mio Kabata,[2] Kanae Mitsunaga,[2] Yohei Mineharu,[3] Sho Ohta,[1] Masato Nakagawa,[2] Susumu Miyamoto,[3] Takuya Yamamoto,[2,4,5] and Yasuhiro Yamada[1,2,4,7,*]

[1]Division of Stem Cell Pathology, Center for Experimental Medicine and Systems Biology, Institute of Medical Science, University of Tokyo, 4-6-1 Shirokanedai, Minato-ku, Tokyo 108-8639, Japan
[2]Department of Life Science Frontiers, Center for iPS Cell Research and Application (CiRA), Kyoto University, 53 Kawahara-cho, Shogoin, Sakyo-ku, Kyoto 606-8507, Japan
[3]Department of Neurosurgery, Kyoto University Graduate School of Medicine, 54 Kawahara-cho, Shogoin, Sakyo-ku, Kyoto 606-8507, Japan
[4]AMED-CREST, AMED 1-7-1 Otemachi, Chiyoda-ku, Tokyo 100-0004, Japan
[5]Institute for the Advanced Study of Human Biology (WPI-ASHBi), Kyoto University, Yoshida-Konoe-cho, Sakyo-ku, Kyoto 606-8501, Japan
[6]These authors contributed equally
[7]Lead Contact
*Correspondence: yasu@ims.u-tokyo.ac.jp
https://doi.org/10.1016/j.celrep.2019.02.009

SUMMARY

Atypical teratoid/rhabdoid tumor (AT/RT), which harbors *SMARCB1* mutation and exhibits a characteristic histology of rhabdoid cells, has a poor prognosis because of the lack of effective treatments. Here, we establish human *SMARCB1*-deficient pluripotent stem cells (hPSCs). *SMARCB1*-deficient hPSC-derived neural progenitor-like cells (NPLCs) efficiently give rise to brain tumors when transplanted into the mouse brain. Notably, activation of an embryonic stem cell (ESC)-like signature confers a rhabdoid histology in *SMARCB1*-deficient NPLC-derived tumors and causes a poor prognosis. Consistently, we find the activation of the ESC-like gene expression signature and an ESC-like DNA methylation landscape in clinical specimens of AT/RT. Finally, we identify candidate genes that maintain the activation of the ESC-like signature and the growth of AT/RT cells. Collectively, *SMARCB1*-deficient hPSCs offer the human models for AT/RT, which uncover the role of the activated ESC-like signature in the poor prognosis and unique histology of AT/RT.

INTRODUCTION

Atypical teratoid/rhabdoid tumor (AT/RT) is an extraordinarily lethal malignant CNS tumor that occurs mainly in early childhood. The representative morphological feature of AT/RT is a population of cells with classic rhabdoid features: eccentrically located nuclei containing vesicular chromatin, prominent eosinophilic nucleoli, abundant cytoplasm with an obvious eosinophilic globular cytoplasmic inclusion, and well-defined cell borders (Louis et al., 2016). Loss of SMARCB1 (also known as INI1, SNF5, or BAF47) expression at the protein level is observed in almost all

AT/RTs, and current consensus holds that immunohistochemical staining for SMARCB1 is a sensitive and specific test for the diagnosis of AT/RT (Louis et al., 2016). Several mouse models of *Smarcb1* ablation have been developed to model AT/RT and rhabdoid tumor (Ng et al., 2015; Han et al., 2016). Genetic ablation of *Smarcb1* at different developmental stages revealed that intracranial tumors with the rhabdoid histology develop only when *Smarcb1* is deleted at embryonic day 6–10 (E6–E10), whereas ablation after birth results in lymphoma development, indicating that a restricted early developmental window is required for the initiation of intracranial rhabdoid tumors (Han et al., 2016). Furthermore, compound deletion of *Smarcb1* and *p53* at *GFAP*-expressing neuronal progenitor cells resulted in the development of AT/RT with rhabdoid histological features. Moreover, the expression profile of mouse and human intracranial rhabdoid tumors revealed the highest correlation with neural progenitors and stem cells (Han et al., 2016). Taken together, these findings suggest that AT/RT may arise from neural stem or progenitor cells.

Patients with AT/RT show a rapid clinical deterioration and extremely worse outcome than those with other CNS tumors, despite aggressive surgical and adjuvant radiochemotherapy. Retrospective and epidemiological studies have demonstrated a mean overall survival ranging from 6 to 18 months (Hilden et al., 2004; von Hoff et al., 2011; Chen et al., 2006). Although intensive multimodality regimens have improved the survival rates for AT/RT patients, AT/RT is still refractory to most treatments (Frühwald et al., 2016). Several preclinical studies attempting to identify molecular targets of AT/RT have taken place in recent years. Particularly, the inhibition of enhancer of zeste homolog 2 (EZH2) has been reported to suppress rhabdoid tumor cell growth, and a clinical trial with a specific inhibitor for EZH2 has been in progress against SMARCB1-defective tumors (Knutson et al., 2013; Alimova et al., 2013; Wilson et al., 2010). Besides expectation of these preclinical studies, the development of effective therapeutic approaches has been desired for this deadly cancer.
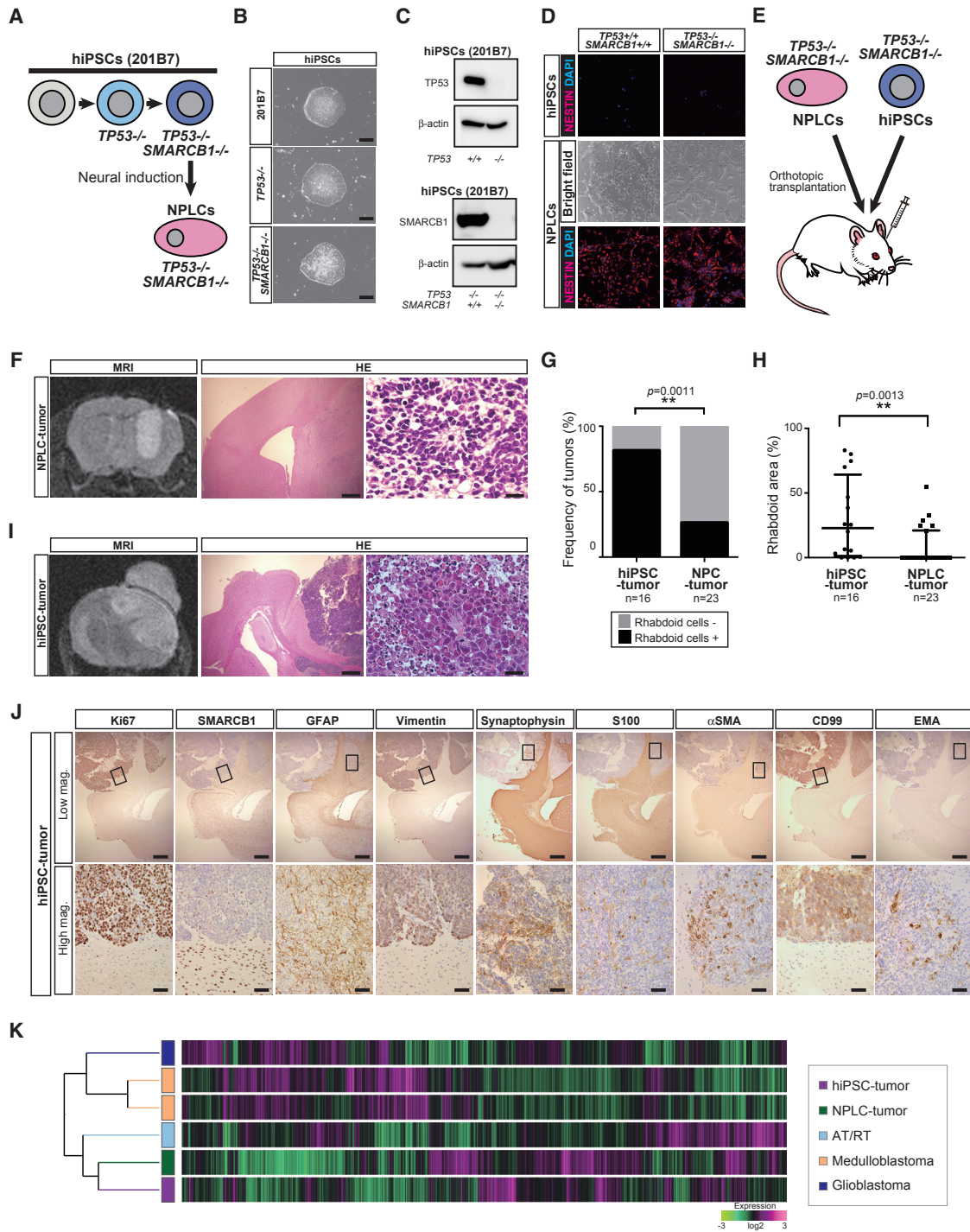
Figure 1. Generation of an Atypical Teratoid/Rhabdoid Tumor Model using hPSCs Lacking *SMARCB1* and *TP53*

(A) A schematic illustration of the establishment of hiPSCs $^{SMARCB1-/-;\ TP53-/-}$ and NPLCs $^{SMARCB1-/-;\ TP53-/-}$.

(B) Representative morphology of hiPSCs, hiPSCs $^{TP53-/-}$ and hiPSCs $^{SMARCB1-/-;\ TP53-/-}$. Scale bars, 200 μm.

(C) The lack of TP53 and SMARCB1 proteins in hiPSCs $^{SMARCB1-/-;\ TP53-/-}$ was confirmed by western blot analysis.

(D) Immunofluorescent staining for NESTIN in hiPSCs $^{SMARCB1-/-;\ TP53-/-}$ and NPLCs $^{SMARCB1-/-;\ TP53-/-}$. NESTIN-expressing cells emerged after neural induction.

(E) A schematic illustration of the xenograft transplantation of hiPSCs or NPLCs into the brain of immunocompromised mice.

(F) MRI and representative histological images of a NPLC $^{SMARCB1-/-;\ TP53-/-}$-derived tumor (NPLC-tumor). NPLCs $^{SMARCB1-/-;\ TP53-/-}$ give rise to brain tumors, which consist of densely packed undifferentiated small blue round cells with rosette formation. Scale bars, 500 μm (left) and 20 μm (right).

(legend continued on next page)

Previous studies have shown that poorly differentiated tumors in humans often exhibit activation of an embryonic stem cell (ESC)-like gene expression signature, which is correlated with a worse prognosis in adults (Ben-Porath et al., 2008; Wong et al., 2008). Consistently, *SALL4,* one of the key factors in the maintenance of pluripotency, is re-expressed in a subset of hepatocellular carcinoma cells, especially in patients who have an unfavorable prognosis, suggesting that the acquisition of ESC-like features plays a role in cancer progression (Yong et al., 2013). Takahashi and Yamanaka (2006) succeeded to confer ESC properties to somatic cells upon the transient expression of four reprogramming factors. Recently, an *in vivo* reprogramming strategy, which enables the fate conversion of differentiated somatic cells to pluripotent stem cells (PSCs) *in vivo*, has been developed (Taguchi and Yamada, 2017). Notably, a premature termination of the *in vivo* reprogramming in mice causes the development of pediatric cancer-like tumors with activation of the ESC-like signature (Ohnishi et al., 2014). In addition, the transient expression of reprogramming factors in *Kras* mutant mice causes the development of alfa-fetoprotein (AFP)-producing cancers, which simultaneously express pluripotency-associated genes and exhibit activation of the ESC-like signature (Shibata et al., 2018). Collectively, activation of the ESC-like signature is involved in the development and progression of particular types of cancer.

Given that PSCs can give rise to various cell types while preserving genetic information, human PSCs (hPSCs) have provided an attractive platform for disease modeling in a genetically defined background in human cells. Indeed, previous studies tried to model human cancers by using hPSCs (Kim et al., 2013; Stricker et al., 2013; Sancho-Martinez et al., 2016), and hESCs with genetic mutation at histone H3.3 succeeded to model diffuse intrinsic pontine glioma in the proper cellular context after neural differentiation (Funato et al., 2014). Here, we established an AT/RT model using human induced pluripotent stem cells (iPSCs) lacking *SMARCB1*. The human iPSC-derived AT/RT model uncovered an unappreciated feature of AT/RT, which could be a therapeutic target.

RESULTS

Generation of an Atypical Teratoid/Rhabdoid Tumor Model using Human iPSCs Lacking *SMARCB1* and *TP53*

A previous mouse study demonstrated that AT/RT-like tumors develop when mutations for both *Smarcb1* and *p53* are intro-duced into neural progenitor cells. In the present study, to establish a human AT/RT model, we introduced genetic mutations at *SMARCB1* and *TP53* into 201B7 human iPSCs (hiPSCs) (hiPSCs $^{SMARCB1-/-;\ TP53-/-}$) using the CRISPR/Cas9 system. We first established hiPSCs deficient of *TP53* alone (hiPSCs $^{TP53-/-}$), and then introduced an additional mutation at *SMARCB1* to generate hiPSCs $^{SMARCB1-/-;\ TP53-/-}$ (Figures 1A–1C). Subsequently, we induced neural differentiation in hiPSCs $^{SMARCB1-/-;\ TP53-/-}$, hiPSCs $^{TP53-/-}$ and control 201B7 hiPSCs (Yan et al., 2013). iPSCs with all genotypes efficiently changed their morphology into neural progenitor-like cells (NPLCs) (Figure 1D). Consistently, *NANOG* and *OCT4* expression were reduced in NPLCs at day 14 of the neural induction (Figure S1A). In contrast, an increased expression of neural progenitor cell (NPC)-related genes, such as *NESTIN*, *NCAM*, and *PAX6*, was observed in these NPLCs (Figures S1A–S1C). However, the expression levels of NPC-related genes were lower in NPLCs with *SMARCB1* deficiency when compared with wild-type control NPLCs (Figure S1A). Further induction of neuronal differentiation in NPLCs confirmed that neuronal differentiation is impaired in *SMARCB1*-deficient cells *in vitro* (Figure S1B). We also examined the effect of *SMARCB1* deficiency on the cell growth of hPSCs and NPLCs *in vitro*. The *TP53* ablation promoted cell proliferation in both hPSCs and NPLCs, whereas the *SMARCB1* ablation inhibited the cell growth of hiPSCs (Figure S1D). Although *SMARCB1* deficiency inhibited neuronal differentiation, it did not increase cell proliferation in NPLCs *in vitro* (Figure S1D).

To test the effect of *SMARCB1* deficiency on the tumor-forming ability of NPLCs *in vivo*, we performed xenograft transplantation of NPLCs $^{SMARCB1-/-;\ TP53-/-}$ and control NPLCs into mouse brain (Figure 1E). The orthotopic transplantation of NPLCs $^{SMARCB1-/-;\ TP53-/-}$ caused the development of aggressive tumors (n = 26/26) (Figures 1F and S1E). In contrast, control 201B7 NPLCs and NPLCs $^{TP53-/-}$ gave rise to only microscopic tumors (n = 2/2, 4/5, respectively) (Figures S1F and S1G), and no macroscopic tumor was developed after the transplantation (n = 0/4, 0/6, respectively) (Figure S1E). Together, *SMARCB1* deficiency markedly promoted tumor formation from NPLCs after orthotopic transplantation *in vivo*.

The histological analysis demonstrated that NPLC $^{SMARCB1-/-;\ TP53-/-}$-derived tumors (hereafter NPLC-derived tumors) were medulloblastoma-like or embryonal tumor with multilayered rosettes (ETMR)-like tumors, which mainly consisted of densely packed undifferentiated small, blue, round

(G) Percentage of tumors with rhabdoid cells. hiPSC-tumors frequently contained rhabdoid cells, whereas a majority of NPLC-tumors did not. **p < 0.01 (Fisher's exact test).

(H) Quantification of the rhabdoid area within a tumor. Note that the rhabdoid area is significantly larger in hiPSC-tumors than NPLC-tumors. Data are represented as the median with interquartile range. **p < 0.01 (Mann-Whitney U test).

(I) MRI and representative histological images of a hiPSC $^{SMARCB1-/-;\ TP53-/-}$-derived tumor (hiPSC-tumor). Note that the hiPSC-tumor contains a number of rhabdoid cells. Scale bars, 500 μm (left) and 20 μm (right).

(J) Immunostaining for Ki67, SMARCB1, GFAP, vimentin, synaptophysin, S100, SMA, CD99, and EMA in a hiPSC-tumor. Tumor cells lack staining for SMARCB1. The majority of hiPSC-tumor cells express Ki67, vimentin, and CD99, while a subset of tumor cells are positive for GFAP, synaptophysin, S100, SMA, and EMA. Scale bars, 500 μm (top) and 50 μm (bottom). Areas in the high-magnification images are shown in the low-magnification images.

(K) Clustering analysis using all probes except for those of lowly expressed genes in a microarray analysis. Global expression profiles in tumors from *SMARCB1*-deficient hiPSCs and NPLCs exhibited similar expression patterns with an AT/RT cell line. Note that medulloblastoma cell lines and a glioblastoma cell line are independently clustered. Microarray data were obtained from GSE45265, GSE36947 (medulloblastomas), and GSE26313 (glioblastoma).

See also Figure S1.
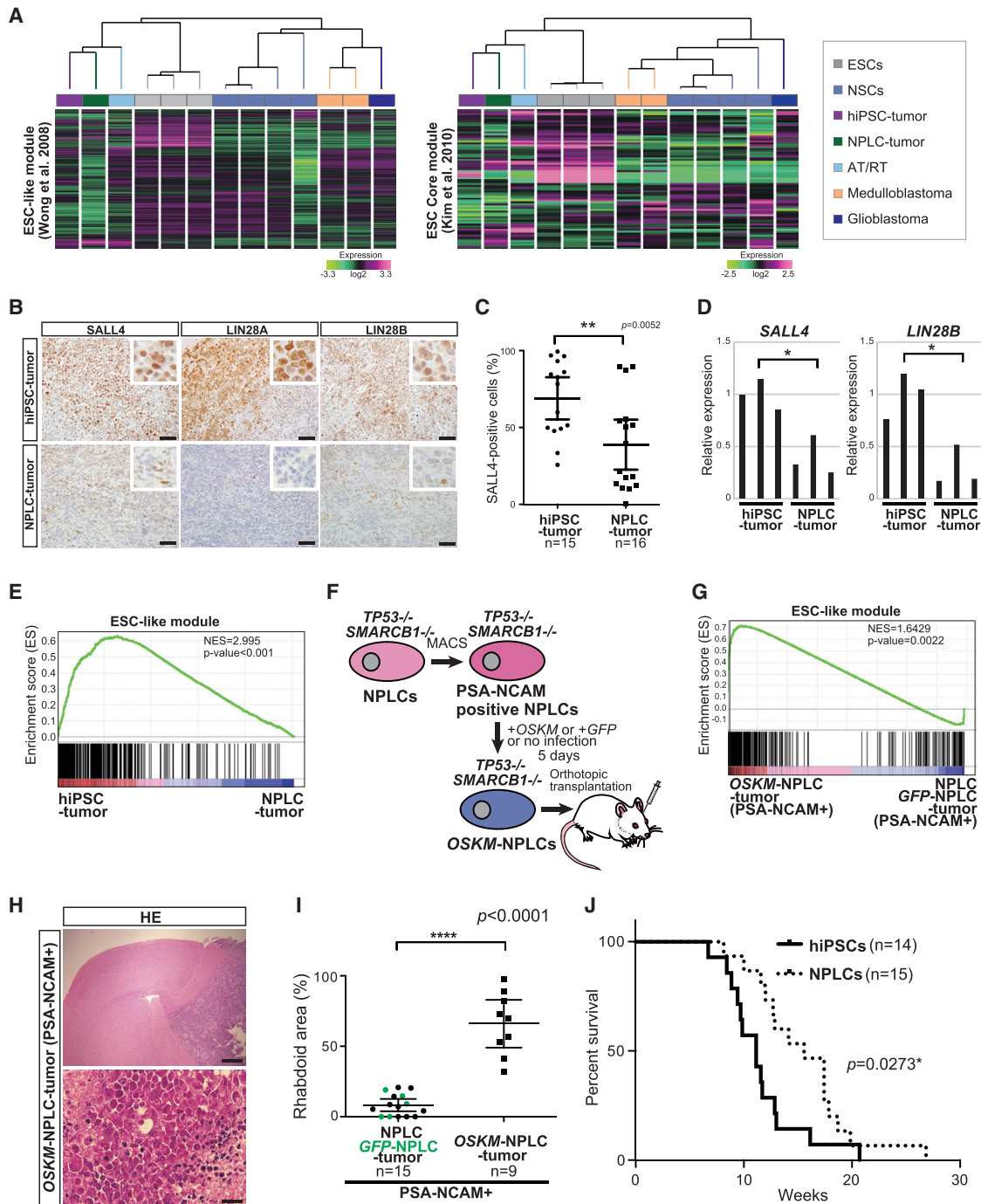
Figure 2. hiPSC-Derived Tumors Exhibit Activation of the ESC-like Gene Expression Signature, which Drives Rhabdoid Tumors *In Vivo*

(A) Clustering analysis using microarray data revealed that both a hESC-like module genes (left) (Wong et al., 2008) and ESC Core module genes (right) (Kim et al., 2010) are similarly expressed in an hiPSC-tumor, a NPLC-tumor, an AT/RT cell line, and hESC lines, whereas medulloblastoma lines and a glioblastoma cell line are clustered with NSCs. The microarray data in Figure 1K were used. Data for NSCs were obtained from GSE18296 and GSE27667.

(B) Immunohistochemical analysis of SALL4, LIN28A, and LIN28B in hiPSC-tumors and NPLC-tumors. Scale bars, 50 μm.

(C) Quantification of the SALL4-positive cells in hiPSC-tumors and NPLC-tumors. Note that hiPSC-tumors contain SALL4-positive cells more frequently than NPLC-tumors. Data are represented as the mean with 95% confidence interval. **p < 0.01 (unpaired t test with Welch's correction).

(D) A qRT-PCR analysis for *SALL4* and *LIN28* expression in hiPSC- and NPLC-tumors. Data are presented as the mean of technical triplicates. The mean expression level of hiPSC-tumors was set to 1. *p < 0.05 (unpaired t test with Welch's correction).

(E) GSEA showing that the ESC-like module is enriched in hiPSC-tumors compared to NPLC-tumors.

(legend continued on next page)

cells with rosettes (Figure 1F). However, the majority of NPLC-derived tumors did not contain rhabdoid cells (Figures 1G and 1H), a characteristic histology of AT/RT. Although NPCs have been suggested to be a cell-of-origin for AT/RT, other studies proposed that pluripotent fetal cells, which are more immature than NPCs, could be an origin based on the morphology in an electron microscope analysis and the unique gene expression in AT/RTs (Bouffard et al., 2004; Deisch et al., 2011). Therefore, we next transplanted hiPSCs $^{SMARCB1-/-; \ TP53-/-}$ without neural induction (Figure 1E). The transplantation of hiPSCs $^{SMARCB1-/-; \ TP53-/-}$ resulted in aggressive tumor formation (n = 18/18) (Figures 1I and S1E), which was similarly observed after the transplantation of NPLCs $^{SMARCB1-/-; \ TP53-/-}$. In contrast, the transplantation of control 201B7 hiPSCs and hiPSCs $^{TP53-/-}$ caused only microscopic tumor formation (n = 2/5 and 1/8, respectively), and no macroscopic tumor formation was observed after the transplantation (Figures S1E and S1F). Notably, the histological analysis demonstrated that hiPSC $^{SMARCB1-/-; \ TP53-/-}$-derived tumors (hereafter hiPSC-derived tumors) frequently contained a large number of rhabdoid cells with vesicular chromatin, prominent nucleoli, and eosinophilic globular cytoplasmic inclusions, which are representative histological features of AT/RT (Figures 1G and 1I). The tumor area with rhabdoid histology was significantly larger in hiPSC-derived tumors than NPLC-derived tumors (Figure 1H). Immunohistochemical analyses revealed that hiPSC-derived tumors exhibit shared features with AT/RT, including high proliferative activity, lack of SMARCB1 expression, and positive staining for vimentin, glial fibrillary acidic protein (GFAP), synaptophysin, CD99, S-100, EMA, and smooth muscle actin (SMA) (Figure 1J). Consistent with the histological observations, clustering analysis of global gene expression revealed that a hiPSC-derived tumor exhibited a similar expression pattern with an AT/RT cell line, whereas medulloblastoma and glioblastoma cell lines fell into a different cluster (Figure 1K). To exclude the possibility of a PSC clone-specific phenotype, we also established an SMARCB1-deficient PSC line by using a different iPSC line, 1383D6 (Figure S1H). The orthotopic transplantation of both 1383D6 iPSCs $^{SMARCB1-/-}$ and 1383D6 NPLCs $^{SMARCB1-/-}$ caused aggressive tumors (5/7 and 5/5, respectively) (Figure S1I), which phenocopied the tumors from 201B7 iPSCs and NPLCs lacking SMARCB1 and TP53. Notably, four out of five 1383D6 iPSC $^{SMARCB1-/-}$-derived tumors contained rhabdoid cells, although the area of the rhabdoid cells was smaller than in 201B7 hiPSC $^{SMARCB1-/-; \ TP53-/-}$-derived tumors (Figures S1I and S1J). In sharp contrast, no rhabdoid

cells were detected in 1383D6 NPLC $^{SMARCB1-/-}$-derived tumors (Figures S1I and S1J). Collectively, we succeeded to model human AT/RT by inoculation of hiPSCs lacking SMARCB1 into mouse brain.

hiPSC-Derived Tumors Exhibit an ESC-like Gene Expression Signature

Our results demonstrating that iPSC-derived tumors exhibited a robust rhabdoid phenotype raised the possibility that a pluripotency-related program is associated with the characteristic rhabdoid histology. Therefore, we next investigated the expression of ESC-related modules in hiPSC- and NPLC-derived tumors together with various brain tumor cell lines. Notably, both hiPSC- and NPLC-derived tumors together with an AT/RT cell line exhibited the ESC-like activation patterns of ESC-related modules, including the ESC Core module, which is composed of genes co-occupied by multiple factors in the core pluripotency network (Figure 2A) (Kim et al., 2010; Wong et al., 2008). We next analyzed the expression of SALL4, LIN28A, and LIN28B, which are associated with the maintenance and acquisition of pluripotency, in hiPSC- and NPLC-derived tumors. Immunohistochemical analysis revealed that both hiPSC- and NPLC-derived tumors expressed SALL4, LIN28A, and LIN28B, but the expression was particularly pronounced in hiPSC-derived tumors (Figures 2B and 2C). We also confirmed the elevated expression of SALL4 and LIN28B in hiPSC-derived tumors by qRT-PCR (Figure 2D). Consistently, gene set enrichment analysis (GSEA) showed an enrichment of the ESC-like module (Wong et al., 2008) in hiPSC-derived tumors compared to NPLC-derived tumors (Figure 2E) (Subramanian et al., 2005). Together, we confirmed the ESC-like signature is activated in hiPSC-derived tumors.

Induction of the ESC-like Signature Leads to Rhabdoid Phenotypes in NPLC-Derived Tumors

To further investigate the role of the pluripotency-related signature in the histogenesis of rhabdoid cells, we next tried to induce the ESC-like signature during tumor development from NPLCs $^{SMARCB1-/-; \ TP53-/-}$ by the forced expression of four reprogramming factors, namely, OCT4, SOX2, KLF4, and c-MYC (OSKM-NPLCs) (Figure S2A). It was reported that the removal of polysialylated-neural cell adhesion molecule (PSA-NCAM)-negative cells could prevent mesodermal tumor formation in hiPSC-derived NPC transplantation, indicating that PSA-NCAM antibody is useful for excluding undifferentiated, tumor-forming PSCs after neural induction (Lee et al., 2015). To eliminate the tumorigenic undifferentiated PSCs after neural induction into NPLCs $^{SMARCB1-/-; \ TP53-/-}$, we sorted neural-differentiated cells with the PSA-NCAM antibody using

(F) A schematic illustration of the xenograft transplantation study. PSA-NCAM-positive NPLCs $^{SMARCB1-/-; \ TP53-/-}$ were sorted by MACS, followed by the retroviral transduction of GFP (GFP-NPLCs) or OSKM (OCT4, SOX2, KLF4, and c-MYC: OSKM-NPLCs) and orthotopic transplantation into the mouse brain.

(G) GSEA showing that the ESC-like module is activated in OSKM-NPLC-tumors compared to control NPLC-tumors.

(H) Representative histological images of an OSKM-NPLC-tumor. A number of rhabdoid cells are observed in the tumor. Scale bars, 500 μm (top) and 20 μm (bottom).

(I) Quantification of the rhabdoid area in OSKM-NPLC-tumors. Note that the rhabdoid areas in OSKM-NPLC-tumors are significantly larger than those in the control NPLC-tumors. Data are represented as the mean with 95% confidence interval. ****p < 0.0001 (unpaired t test with Welch's correction).

(J) Survival curve of mice transplanted with hiPSCs $^{SMARCB1-/-; \ TP53-/-}$ or NPLCs $^{SMARCB1-/-; \ TP53-/-}$. The overall survival of hiPSC $^{SMARCB1-/-; \ TP53-/-}$-transplanted mice is shorter than NPLC $^{SMARCB1-/-; \ TP53-/-}$-transplanted mice. Kaplan-Meier analysis was performed. *p < 0.05 (log-rank test).

See also Figure S2.

magnetic-activated cell sorting (MACS). We confirmed the high efficiency of MACS of PSA-NCAM-positive cells by a flow cytometric analysis (Figure S2B). OCT4, SOX2, KLF4, and c-MYC were retrovirally transduced into NPLCs or PSA-NCAM-positive NPLCs (Figure S2C), and the OSKM-NPLCs were inoculated into the mouse brain to obtain NPLC-derived tumors (Figures 2F and S2A). All mice transplanted with OSKM-NPLCs developed aggressive brain tumors (n = 9). Although OSKM-NPLCs did not exhibit a prominent upregulation of pluripotency-related genes in vitro (Figure S2D), an enrichment of the ESC-like module was observed in OSKM-NPLC-derived tumors when compared to control NPLC-derived tumors (Figure 2G), suggesting that OSKM induction conferred the ESC-like gene expression signature in NPLC-derived tumors (Wong et al., 2008). Of particular note, OSKM-NPLC-derived tumors exhibited an apparent rhabdoid histology in most areas (Figure 2H). Consistently, the rhabdoid area in OSKM-NPLC-derived tumors was significantly larger than that in control NPLC-derived tumors (Figure 2I). Collectively, we concluded that activation of the ESC-like signature is responsible for the characteristic rhabdoid histology.

Orthotopic Transplantation of hiPSCs $^{SMARCB1-/-; TP53-/-}$ Results in Poor Survival Compared to NPLC $^{SMARCB1-/-; TP53-/-}$ Transplantation

Previous studies demonstrated that activation of the ESC-like signature in tumors is associated with a worse prognosis of adult cancer patients (Ben-Porath et al., 2008). Therefore, we next investigated the survival period of mice after the orthotopic transplantation of hiPSCs $^{SMARCB1-/-; TP53-/-}$ and NPLCs $^{SMARCB1-/-; TP53-/-}$. Consistent with a positive correlation between activation of the ESC-like signature and the poor prognosis, the overall survival of hiPSC $^{SMARCB1-/-; TP53-/-}$-transplanted mice that developed tumors with rhabdoid histology was substantially shorter than NPLC $^{SMARCB1-/-; TP53-/-}$-transplanted mice (Figure 2J). Similarly, mice inoculated with OSKM-NPLCs, which also developed tumors with rhabdoid histology, exhibited poor survival when compared to mice inoculated with control NPLCs (Figures S2E and S2F). Together, these results indicate that activation of the ESC-like signature is associated with a worse prognosis of SMARCB1-deficient tumors.

c-MYC Induces Activation of the ESC-like Signature in NPLC-Derived Tumors and Drives Rhabdoid Tumor Development In Vivo

Our results indicate that activation of the ESC-like signature is associated with the unique rhabdoid histology and poor prognosis of AT/RT. However, how AT/RT cells acquire the ESC-like signature remains unclear. A previous study demonstrated that c-Myc activates the ESC-like signature in adult epithelial cells and cancer cells and increases the fraction of tumor-initiating cells (Wong et al., 2008). Considering that c-MYC is overexpressed in a subset of AT/RTs (Johann et al., 2016), we next investigated the effect of c-MYC induction on the activation of the ESC-like signature and the rhabdoid phenotype in NPLC-derived tumors. c-MYC was retrovirally transduced in NPLCs $^{SMARCB1-/-; TP53-/-}$ or PSA-NCAM-positive NPLCs $^{SMARCB1-/-; TP53-/-}$ (MYC-NPLCs), and then MYC-NPLCs were inoculated into mouse brain (Figures 3A, S3A,

and S3B). Notably, MYC-NPLCs gave rise to aggressive tumors containing a large number of rhabdoid cells (Figures 3B, 3C, S3C and S3D). Moreover, these tumors exhibited an activation of ESC-like module genes (Figure 3D) and increased expression of SALL4 and LIN28 (Figure 3E) compared to control tumors.

To investigate the effect of c-MYC overexpression on the disease outcome, we next investigated the survival period of mice transplanted with MYC-NPLCs. The overall survival of these mice was significantly shorter than that of controls (Figures 3F and S3E). Collectively, these results demonstrate that c-MYC overexpression alone is sufficient for activation of the ESC-like signature and rhabdoid histology in NPLC-derived tumors, which was linked to a worse prognosis.

Activation of the ESC-like Gene Expression Signature in Human AT/RT Specimens

Above, we showed that activation of the ESC-like signature is related to the emergence of rhabdoid cells, a unique histological feature of AT/RT, and the worse prognosis of NPLC $^{SMARCB1-/-; TP53-/-}$-transplanted mice. We next examined the gene expression profile of clinical samples of human AT/RTs, medulloblastomas, and glioblastomas by using previously published datasets. Clustering analysis revealed that ESC-like module genes (Wong et al., 2008) are similarly activated in AT/RT samples and ESCs and iPSCs, whereas medulloblastomas and glioblastomas fall into a different cluster (Figure 4A). Similar results were obtained in the clustering analysis using the ESC Core module (Figure 4A) (Kim et al., 2010). We also examined activation of the ESC-like signature in ETMRs, which often show LIN28A immunoreactivity. Notably, some ETMRs also exhibited ESC-like activation of the ESC Core module genes (Figure S4A). Consistent with the ESC-like gene expression signature, the expression of SALL4, LIN28A, and LIN28B were elevated in AT/RTs compared to glioblastomas (Figure 4B). SALL4 was highly expressed in AT/RTs compared with medulloblastomas, but the expression level of LIN28B was higher in medulloblastomas (Figure 4B). The increased expression of SALL4, LIN28A, and LIN28B were also confirmed in AT/RT clinical specimens by immunohistochemistry (Figure S4B) (Deisch et al., 2011) (Weingart et al., 2015). Taken together, we confirmed that human AT/RTs harbor the ESC-like signature.

ESC-like DNA Methylation Landscape in Human AT/RT Specimens

Given that human AT/RTs exhibit the ESC-like gene expression signature, we next examined DNA methylation patterns between AT/RTs and PSCs. We performed a comprehensive genome-wide methylation analysis of CpG islands (CGIs) in AT/RTs together with other brain tumors by using previously published datasets. In this analysis, we first extracted CpG sites within CGIs or around transcription start sites (TSSs; ± 1,500 bp), which are differentially methylated between PSCs and adult brain tissues (DNAme difference [Dif], >0.6), and then examined DNA methylation levels in AT/RTs, medulloblastomas, ETMRs, glioblastomas, fetal brain tissues, and neural stem cells (NSCs). We found that CGI methylation levels at brain-unmethylated sites (PSC-methylated sites) are often increased in AT/RTs but
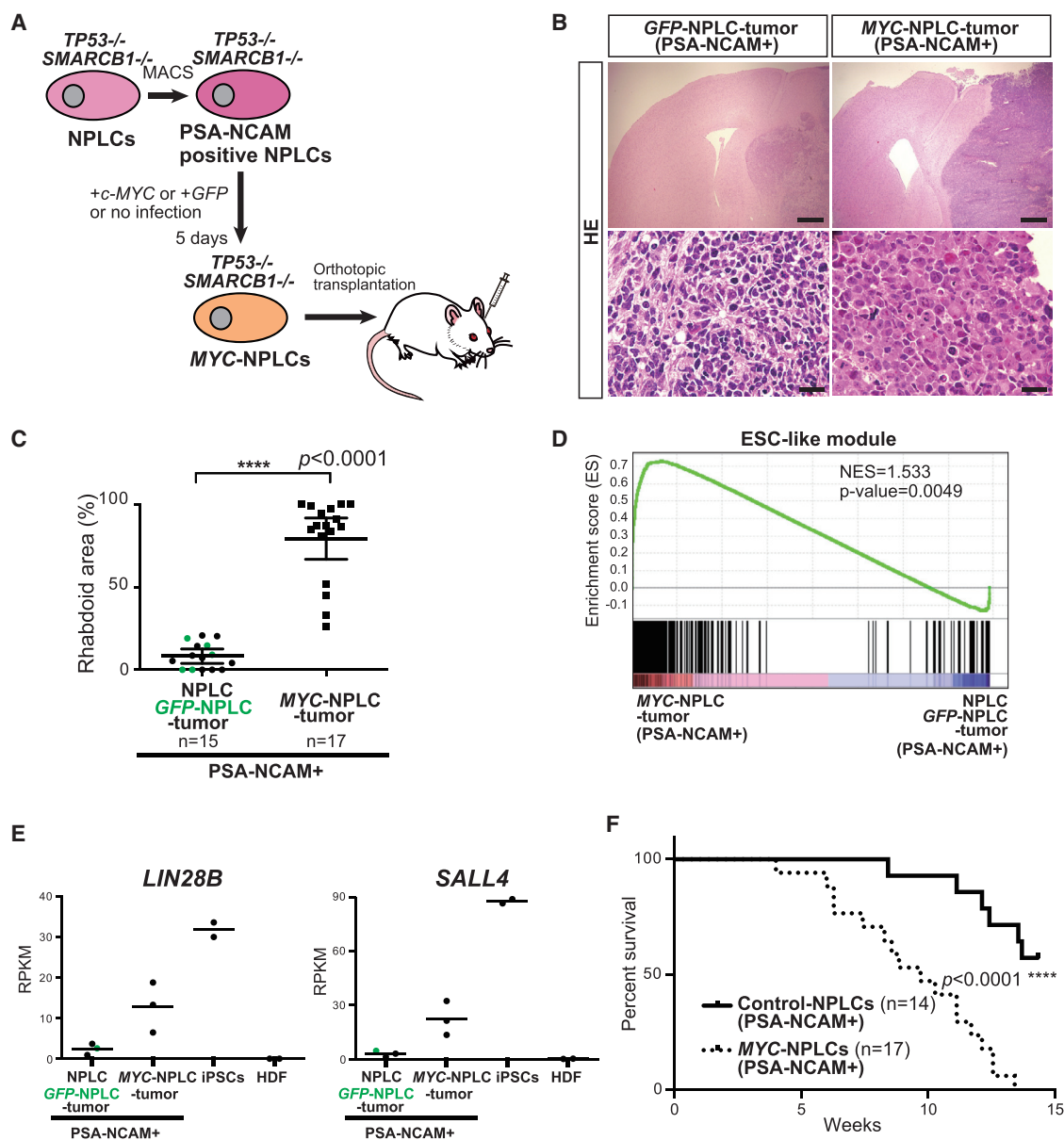
Figure 3. c-*MYC* Induces Activation of the ESC-like Signature and Drives Rhabdoid Tumors *In Vivo*

(A) A schematic illustration of the xenograft transplantation study. PSA-NCAM-positive NPLCs $^{SMARCB1-/-;\ TP53-/-}$ were sorted by MACS and then retrovirally transduced with *GFP* (*GFP*-NPLC) or c-*MYC* (*MYC*-NPLC), which were transplanted into the mouse brain. The control NPLCs are the same as Figure 2F.

(B) Representative histological images of *GFP*-NPLC-tumors and *MYC*-NPLC-tumors. *MYC*-NPLC-tumors contain rhabdoid cells. Scale bars, 500 μm (top) and 20 μm (bottom).

(C) Quantification of the rhabdoid area in NPLC-tumors. Note that the rhabdoid area in *MYC*-NPLC-tumors is significantly larger than in control NPLC-tumors. Data are represented as the mean with 95% confidence interval. ****p < 0.0001 (unpaired t test with Welch's correction).

(D) GSEA showing that the ESC-like module is enriched in *MYC*-NPLC-tumors compared to control NPLC-tumors.

(E) Expression levels of *LIN28B* and *SALL4* in *MYC*-NPLC-tumors, control NPLC-tumors, iPSCs, and human dermal fibroblasts (HDF) by RNA sequencing (RNA-seq) analysis. Lines indicate mean expression values. RPKM, reads per kilobase of exon per million mapped sequence reads.

(F) Survival curves of mice transplanted with *MYC*-NPLCs or control NPLCs. The overall survival of mice inoculated with *MYC*-NPLCs is significantly shorter than of controls. Kaplan-Meier analysis was performed. ****p < 0.0001 (log-rank test).

See also Figure S3.

not so much in other tumors or NSCs (Figures 4C and S5). Although ETMRs exhibited the ESC-like gene expression signature, PSC-methylated sites remain unmethylated in ETMRs (Figure S5). In contrast, CGI methylation levels at adult brain-specifically methylated sites tended to be decreased in AT/RTs but not in other tumors, including ETMRs compared to adult
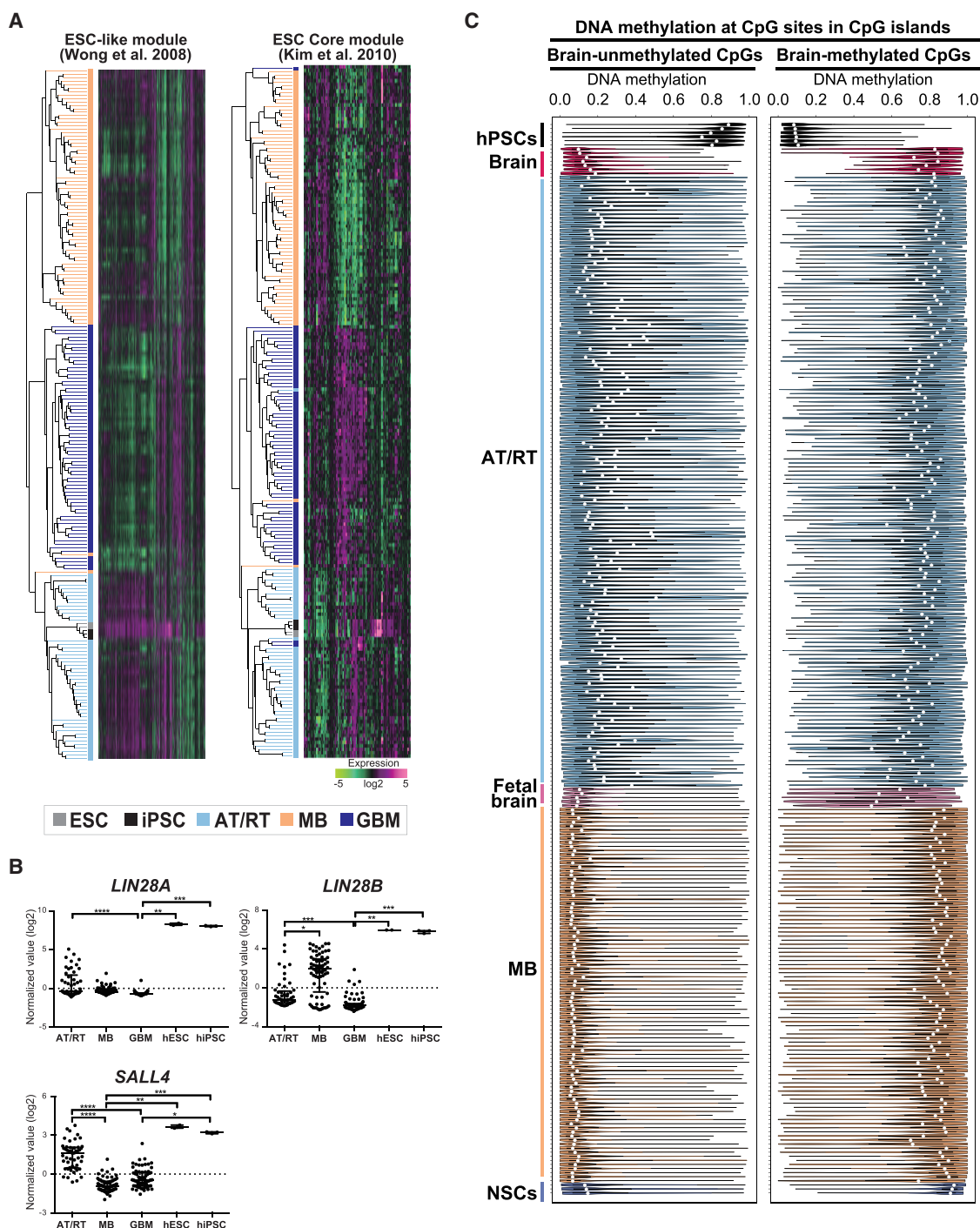
Figure 4. Human AT/RT Specimens Exhibit Activation of the ESC-like Gene Expression Signature and ESC-like DNA Methylation Landscape

(A) Clustering analysis using microarray data revealed that both hESC-like module genes (left) and ESC Core module genes (right) are similarly expressed in AT/RT samples and ESCs and iPSCs. Note that medulloblastoma (MB) and glioblastoma (GBM) samples are clustered separately from ESCs and iPSCs. Microarray data of hPSCs, AT/RTs, medulloblastomas, and glioblastomas were obtained from GSE22392 (hESC/hiPSC), GSE70678 (AT/RT), GSE37418 (MB), and GSE53733 (GBM).

(B) Expressions of *SALL4* and *LIN28* in AT/RTs, medulloblastomas, and glioblastomas compared to ESCs and iPSCs. Data are represented as the median with interquartile range. *p < 0.05, **p < 0.01, ***p < 0.001, ****p < 0.0001 (Kruskal-Wallis test and Dunn's multiple comparisons test). The same microarray data as Figure 4A were used.

(C) The DNA methylation landscape in AT/RTs analyzed using Infinium450K data. In this analysis, we first extracted differentially methylated CpG sites within CpG islands (CGIs) between hPSCs and adult brains. hPSC-specific methylated CpG sites and adult brain-specific methylated CpG sites within CGIs were analyzed

(legend continued on next page)

brain tissues or NSCs (Figures 4C and S5). Similar patterns of DNA methylation alterations were observed at CpG sites around TSSs (Figure S5). Taken together, we concluded that AT/RTs harbor an ESC-like DNA methylation landscape.

Pediatric Cancers Exhibit Activation of the ESC-like Gene Expression Signature

Previous studies demonstrated that pluripotency-related genes, such as *LIN28B*, are frequently upregulated in other pediatric cancers that occur in early childhood, which raised the possibility that activation of the ESC-like signature is a shared feature in pediatric cancers. Therefore, we next examined the expression of the ESC-like module genes in three other pediatric cancers, namely, neuroblastoma (NB), Wilms' tumor (WT), and hepatoblastoma (HB), by comparing them with their corresponding adult cancer, namely, adrenocortical carcinoma (ACC), renal cell carcinoma (RCC), and hepatocellular carcinoma (HCC), respectively. Notably, a principal-component analysis (PCA) revealed that all three pediatric cancer types exhibited similar expression profiles with PSCs and activation of the ESC-like module genes compared to the corresponding adult cancers (Figures 5A and S6). Consistently, the pediatric cancers showed increased expression of *SALL4* and *LIN28B* compared to their counterparts (Figure 5B). Together, our data indicate that activation of the ESC-like signature is a common characteristic of pediatric cancers.

Genetic Screening with CRISPR/Cas9 to Develop a Strategy for AT/RT Therapy

Our findings about activation of the ESC-like signature suggest the signature could make a promising therapeutic target for AT/RT. Therefore, we performed genetic screening to identify genes that play a role in the malignant features of AT/RT (Figure 6A). Accordingly, we picked out 110 target genes that are associated with the maintenance of ESC identity based on previous reports (Tables S1 and S2). A lentiviral CRISPR/Cas9 system was employed to disrupt the candidate genes in a cancer cell line, which was established from hiPSC-derived tumors (Figure 6A; Table S1). The high efficiency of non-homologous end joining by this lentiviral CRISPR/Cas9 system was confirmed 7 days after lentiviral transduction in the pediatric cancer cell line SK-N-BE(2) (Figure S7A). The genetic screening revealed decreased cancer cell growth after the transduction of CRISPR/Cas9 together with single guide RNA (sgRNA) for dozens of genes compared to non-targeting control (NTC) sgRNA (Figure 6B; Table S3). Notably, among the candidate genes was *Enhancer of zeste homolog 2* (*EZH2*), which has been reported as a target of AT/RT treatment (Knutson et al., 2013; Alimova et al., 2013; Wilson et al., 2010), indicating that our screening successfully identified potential therapeutic targets. Indeed, we confirmed that GSK126, a specific inhibitor for EZH2, efficiently suppressed growth of the hiPSC-derived

cancer cell line. Moreover, GSK126 efficiently inhibited the ESC-like signature in the hiPSC-derived cancer cell line (Figure S7B).

Given that other pediatric cancers similarly exhibit activation of the ESC-like signature, we also performed the same genetic screening in two neuroblastoma cell lines, namely, SK-N-AS and SK-N-BE(2). We found that *RAD21* knock out efficiently reduced cell proliferation in the hiPSC-derived cancer cell line and neuroblastoma cell lines (Figures 6B and 6C). The inhibitory effect of cell growth was confirmed in another guide RNA targeting RAD21 (Figure S7C). Notably, *RAD21* as well as *EZH2* was highly expressed in AT/RTs compared to glioblastomas (Figure 6D). Moreover, the increased expression of *RAD21* and *EZH2* was similarly observed in other pediatric cancers, including neuroblastomas, Wilms' tumors, and hepatoblastomas, when compared to the corresponding adult cancers (Figure 6E). Therefore, we focused on *RAD21* and *EZH2* and conducted further experiments.

The inhibitory effect on tumor cell growth in the hiPSC-derived cancer cell line by the knockout of *RAD21* and *EZH2* was validated in a large-scale culture (Figure 6F). Xenograft experiments revealed that the lentiviral CRISPR/Cas9-mediated knock out of *RAD21* or *EZH2* extended the overall survival of mice after the inoculation of hiPSC-derived cancer cells (Figures 6G and 6H). Therefore, we concluded that *RAD21* and *EZH2* are potential therapeutic targets for AT/RTs.

RAD21 is a key central component within the multi-protein cohesin complex. A previous study demonstrated that histone deacetylase 8 (HDAC8) functions as a deacetylase of SMC3, another component of the cohesin complex, and plays a role in recycling cohesin during cell division (Deardorff et al., 2012). Moreover, it was shown that PCI34051, a HDAC8-specific inhibitor, reduces the localized cohesin, indicating that the inhibitor impairs cohesin function. Considering that *RAD21* knock out inhibited cancer cell growth in the AT/RT model, we next investigated the effect of PCI34051 on cancer cell growth in this model. PCI34051 treatment resulted in a modest reduction in the cell growth of hiPSC-derived cancer cells (Figures 6I and S7D). The growth inhibitory effect was not obvious in the presence of *siRAD21*, which supports the notion that PCI34051 inhibits cell growth by impairing cohesin function (Figure S7D). Most notably, simultaneous treatment with PCI34051 and GSK126 markedly inhibited the cell proliferation (Figure 6I). Mechanistically, suppression of the ESC-like gene expression signature by GSK126 was more pronounced by the combination treatment of PCI34051 and GSK126 (Figures 6J and S7E), although PCI34051 alone did not significantly suppress the ESC-like signature (Figure S7F). Consistently, a gene ontology enrichment analysis revealed that the combination treatment induced genes associated with nervous system development (Figure 6K), suggesting that the combined inhibition of HDAC8 and EZH2 induced neuronal differentiation. We also confirmed that the

A

ESC-like module
(Wong et al. 2008)

ESC Core module
(Kim et al. 2010)

B

LIN28B

SALL4

combination treatment remarkably suppressed proliferation in other rhabdoid and AT/RT cell lines (Figure 6L), as well as neuroblastoma cell lines (Figure 6M). In sharp contrast, the suppressive effect was not prominent in two of three glioblastoma cell lines (Figure S7G), which is consistent with the fact that most glioblastomas do not exhibit activation of the ESC-like signature.

DISCUSSION

In the present study, we established hPSCs deficient for *SMARCB1* to model AT/RT. Although previous studies suggested that NPCs are a cell-of-origin for AT/RT, the majority of tumors from *SMARCB1*-deficient NPLCs lacked typical rhabdoid cells. On the other hand, despite having the same genetic abnormality, the transplantation of *SMARCB1*-deficient hPSCs caused tumors containing a large number of rhabdoid cells, indicating that PSC-related embryonic cell properties are associated with the histogenesis of rhabdoid cells, which was further supported by the fact that forced activation of the ESC-like signature confers the rhabdoid histology in *SMARCB1*-deficient NPLC-derived tumors. Consistent with that notion, we found activation of the ESC-like signature in clinical speci-

mens of AT/RTs but not in medulloblastomas or glioblastomas. Of particular note, *SMARCB1*-deficient hPSC-transplanted mice showed poor survival compared to *SMARCB1*-deficient NPLC-transplanted mice, indicating a positive correlation between activation of the ESC-like signature and poor prognosis. Collectively, we developed a human AT/RT model using hPSCs and identified activation of the ESC-like signature as an important determinant of the unique histology and poor prognosis of AT/RT.

The fact that rhabdoid histology is prominent in PSC-derived tumors compared to NPLC-derived tumors suggests that an earlier embryonic program than the NPC program is involved in the unique histology. However, it remains unclear how AT/RT cells acquire the ESC-like signature in the postnatal brain. Notably, we found that ESC-methylated CpG sites are unmethylated in NSCs and fetal brains, suggesting that the ESC-like methylation patterns in AT/RTs do not simply reflect the DNA methylation patterns in NSCs or fetal cells. These findings may support the assumption that the ESC-like signature is acquired during AT/RT development. It is also interesting to note that genetic ablation of *TP53* seems to enhance the emergence of the rhabdoid histology, although clinical AT/RTs hardly harbor the *TP53* mutation. Given that the loss of *TP53* greatly promotes somatic cell reprogramming into iPSCs (Hong et al., 2009), it is possible that *TP53* deficiency contributed to the acquisition of the ESC-like signature by accelerating the reprogramming
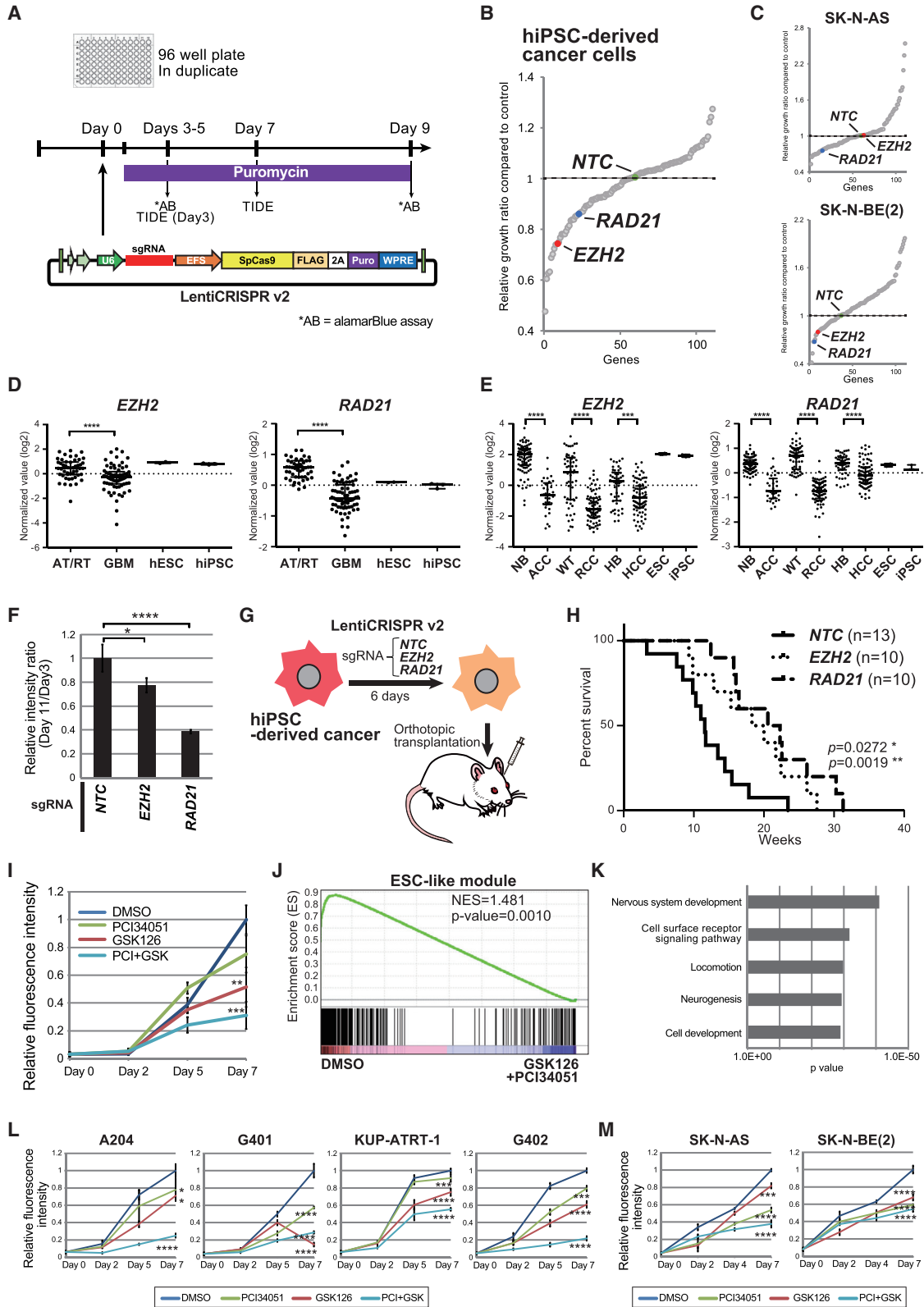
(legend on next page)

process in this particular model. In contrast, we found that *TP53* deficiency alone did not promote the tumor formation *in vivo*, suggesting that the *TP53* deficiency enhances tumor formation in conjunction with *SMARCB1* deficiency.

Notably, we showed that *c-MYC* overexpression induces activation of the ESC-like signature in NPLC-derived tumors and drives tumor development with the rhabdoid phenotype. A previous study demonstrated that *c-MYC* activates the embryonic transcriptional program and causes stem cell-like phenotypes (Wong et al., 2008). Moreover, a recent study demonstrated that *c-MYC*-driven dedifferentiation supports the onset of a stem cell-like state and tumorigenesis in mammary epithelial cells (Poli et al., 2018). Together, we propose that *c-MYC* induces dedifferentiation and activates the ESC-like signature during tumor development from *SMARCB1*-deficient NPLCs. The fact that *c-MYC* is frequently amplified in AT/RT in patients at higher age (Johann et al., 2016) may further support the notion that *c-MYC* induces dedifferentiation during AT/RT development.

Taking advantage of our human AT/RT model, we showed that activation of the ESC-like signature is correlated with the poor prognosis, which raised the possibility that the ESC-like signature is a promising therapeutic target for AT/RT. Accordingly, we performed a CRISPR/Cas9 knock out screening targeting the maintenance of ESC identity and identified genes that potentially maintain the growth of tumor cells. Notably, the identified genes included *EZH2*, which was previously reported as a potential therapeutic target in AT/RT (Choi et al., 2016; Weingart et al., 2015). Importantly, we found that an EZH2 inhibitor efficiently inhibited the ESC-like signature in AT/RT cells, which is consistent with a previous study that demonstrated *Ezh2* maintains the stem cell-associated signature in *Smarcb1*-deficient mouse embryonic fibroblasts (Wilson et al., 2010).

We also found that knock out of *RAD21*, which encodes a component within the cohesin complex, significantly suppresses the growth of AT/RT cells, suggesting that the function of cohesin too could be a target for AT/RT treatment. Consistently, an HDAC8-specific inhibitor, which indirectly reduces localized cohesin, together with the EZH2 inhibitor synergistically inhibited activation of the ESC-like signature and markedly suppressed the proliferation of AT/RT cells but had minimal effect on glioblastoma cells. Although a mechanistic basis for the potent inhibition of the ESC-like signature by the combined inhibition of EZH2 and HDAC8 remains to be solved, we propose that inhibition of the ESC-like signature is an effective strategy for AT/RT treatment.

It is interesting that activation of the ESC-like signature was similarly detectable in other pediatric cancers, such as neuroblastomas, Wilms' tumors, and hepatoblastomas. Notably, the same knock out screening in neuroblastoma cell lines revealed that knock out of *RAD21* often suppressed the growth of neuroblastoma cells. Furthermore, the combined treatment with EZH2 and HDAC8 inhibitors synergistically reduced the proliferation of neuroblastoma cells. Together with previous findings that partial reprogramming *in vivo* induces activation of the ESC-like signature and causes the development of cancers that resemble pediatric cancers (Ohnishi et al., 2014), it is possible that activation of the ESC-like signature may be a general driver of pediatric

Figure 6. CRISPR/Cas9-Mediated Genetic Screening to Develop a Therapeutic Strategy for AT/RT

(A) A schematic illustration of the genetic screening with the lentiviral CRISPR/Cas9 system. An alamarBlue assay was performed to evaluate cell viability. The LentiCRISPR-transduced cell population was examined at days 3–5 and then used for the adjustment to determine the cell growth ratio at day 9. The average of the duplicate values was used for each assay.

(B) The results of a genetic screening of the hiPSC $^{SMARCB1-/-; TP53-/-}$-derived cancer cell line. The transduction of CRISPR/Cas9 with sgRNA targeting *EZH2* and *RAD21* inhibited cell growth.

(C) The results of a genetic screening of the neuroblastoma cell lines SK-N-AS and SK-N-BE(2). The LentiCRISPR-transduced cell population was examined at days 3 and 4, then used for the adjustment to determine the cell growth ratio at days 7–12. The transduction of CRISPR/Cas9 with sgRNA for *RAD21* inhibited cell proliferation in both cell lines.

(D) The expression of *EZH2* and *RAD21* in AT/RTs and glioblastomas. The increased expressions of both *EZH2* and *RAD21* were observed in AT/RTs compared to glioblastomas. The same microarray data as Figure 4A were used. ****p < 0.0001 (Kruskal-Wallis test and Dunn's multiple comparisons test).

(E) The expression of *EZH2* and *RAD21* in pediatric cancers and the corresponding adult cancers. Note that the increased expressions of *RAD21* and *EZH2* were similarly observed in other pediatric cancers. Data are represented as the median with interquartile range. ***p < 0.001, ****p < 0.0001 (Mann-Whitney U test). The same microarray data as Figure 5A were used.

(F) Growth ratios (day 11/day 3) of hiPSC-derived cancer cells transduced with CRISPR/Cas9 with sgRNA for non-targeting control (NTC), *EZH2*, or *RAD21*. The transduction of CRISPR/Cas9 with sgRNA for *EZH2* and *RAD21* reduced the cell growth ratio compared to *NTC*. Data are presented as the mean of three biological replicates with standard deviation. The growth ratio of *NTC*-transduced cells was set to 1. *p < 0.05, ****p < 0.0001 (Kruskal-Wallis test and Dunn's multiple comparisons test).

(G) A schematic illustration of the xenograft transplantation study of hiPSC-derived cancer cells transduced with lentiCRISPR/Cas9 together with sgRNA for *NTC*, *EZH2*, or *RAD21*.

(H) Survival curves of mice transplanted with hiPSC-derived cancer cells transduced with CRISPR/Cas9 and sgRNA for *NTC*, *EZH2*, or *RAD21*. Kaplan-Meier analysis was performed. *p < 0.05, **p < 0.01 (log-rank test).

(I) Cell viability of hiPSC-derived cancer cells treated with DMSO, PCI34051 (10 μM), GSK126 (10 μM), or a combination of PCI34051 and GSK126 (10 μM each). Note that the inhibitory effect is markedly enhanced by the combination treatment. **p < 0.01, ***p < 0.001 (one-way ANOVA and Dunnett's multiple comparisons test).

(J) GSEA showing the suppression of the ESC-like module by the combined treatment of PCI34051 and GSK126 compared to DMSO treatment in hiPSC-derived cancer cells.

(K) Gene ontology enrichment analysis showing that the combined treatment of PCI34051 and GSK126 resulted in the induction of genes associated with neuronal development in hiPSC-derived cancer cells. Genes showing ≥1.5-fold changes compared to DMSO-treated cells were used in the analysis.

(L) Cell viability of rhabdoid cell lines treated with DMSO, PCI34051 (10 μM), GSK126 (10 μM), or the combination of PCI34051 and GSK126 (10 μM each). *p < 0.05, ***p < 0.001, ****p < 0.0001 (one-way ANOVA and Dunnett's multiple comparisons test).

(M) Cell viability of neuroblastoma cell lines treated with DMSO, PCI34051 (10 μM), GSK126 (10 μM), or the combination of PCI34051 and GSK126 (10 μM each). ***p < 0.001, ****p < 0.0001 (one-way ANOVA and Dunnett's multiple comparisons test).

See also Figure S7 and Table S1.

cancer development and, therefore, could be a therapeutic target for pediatric cancers. Indeed, previous studies showed that EZH2 inhibitors are often effective for pediatric cancers (Chen et al., 2018) and that an HDAC8 inhibitor suppresses cell proliferation and induces differentiation in neuroblastoma cells (Oehme et al., 2009). Collectively, we propose that the combined inhibition of EZH2 and HDAC8 could be a promising strategy to treat pediatric cancers by targeting the ESC-like signature.

In summary, we established a human AT/RT model using *SMARCB1*-deficient hPSCs. Taking advantage of the AT/RT model, we unveiled that activation of the ESC-like signature plays a central role in the unique rhabdoid histology and poor prognosis of AT/RT. Finally, we showed that this signature could be a promising therapeutic target for AT/RT as well as other pediatric cancers.

STAR★METHODS

Detailed methods are provided in the online version of this paper and include the following:

- KEY RESOURCES TABLE
- CONTACT FOR REAGENT AND RESOURCE SHARING
- EXPERIMENTAL MODEL AND SUBJECT DETAILS
  - Mice
  - Cell culture and neural induction
  - Establishment of hiPSC $^{SMARCB1-/-;\ TP53-/-}$ -derived cancer cell line
- METHOD DETAILS
  - TP53 and SMARCB1 knockout using CRISPR/Cas9 system
  - Retroviral transduction
  - Xenograft tumor model
  - Histological analysis and immunostaining
  - Immunofluorescent staining
  - Western blot analysis
  - Magnetic-based cell sorting (MACS) and flow cytometric analysis
  - Genetic screening with lentiviral CRISPR/Cas9 system
  - Cell growth inhibition assays and cell proliferation assays
  - siRNA transfection
  - RNA Preparation, qRT-PCR and microarray analysis
  - Library preparation for RNA sequencing
  - RNA-seq data analyses
  - DNA methylation analyses for infinium methylation array data
  - Quantification and Statistical Analysis
- DATA AND SOFTWARE AVAILABILITY

SUPPLEMENTAL INFORMATION

Supplemental Information can be found with this article online at https://doi.org/10.1016/j.celrep.2019.02.009.

ACKNOWLEDGMENTS

We are grateful to Prof. J. Takahashi and Dr. N. Sano for providing the transplant instruments and Drs. Y. Sogabe and K. Semi for support and useful

AUTHOR CONTRIBUTIONS

Y.T., N.J., and Yasuhiro Yamada proposed the research project, designed the experiments, performed the experiments, and wrote the manuscript. M.S., Yosuke Yamada, and T.U. performed the experiments. T.Y., M.K., and S.O. analyzed the microarray and RNA-sequencing data. S.M., Y.A., M.N., Y.M., K.M., and Y.M. provided materials and technical instructions.

DECLARATION OF INTERESTS

The authors declare no competing interests.

REFERENCES

Alimova, I., Birks, D.K., Harris, P.S., Knipstein, J.A., Venkataraman, S., Marquez, V.E., Foreman, N.K., and Vibhakar, R. (2013). Inhibition of EZH2 suppresses self-renewal and induces radiation sensitivity in atypical rhabdoid teratoid tumor cells. Neuro-oncol. *15*, 149–160.

Ben-Porath, I., Thomson, M.W., Carey, V.J., Ge, R., Bell, G.W., Regev, A., and Weinberg, R.A. (2008). An embryonic stem cell-like gene expression signature in poorly differentiated aggressive human tumors. Nat. Genet. *40*, 499–507.

Bouffard, J.P., Sandberg, G.D., Golden, J.A., and Rorke, L.B. (2004). Double immunolabeling of central nervous system atypical teratoid/rhabdoid tumors. Mod. Pathol. *17*, 679–683.

Brinkman, E.K., Chen, T., Amendola, M., and van Steensel, B. (2014). Easy quantitative assessment of genome editing by sequence trace decomposition. Nucleic Acids Res. *42*, e168.

Chen, Y.W., Wong, T.T., Ho, D.M., Huang, P.I., Chang, K.P., Shiau, C.Y., and Yen, S.H. (2006). Impact of radiotherapy for pediatric CNS atypical teratoid/rhabdoid tumor (single institute experience). Int. J. Radiat. Oncol. Biol. Phys. *64*, 1038–1043.

Chen, L., Alexe, G., Dharia, N.V., Ross, L., Iniguez, A.B., Conway, A.S., Wang, E.J., Veschi, V., Lam, N., Qi, J., et al. (2018). CRISPR-Cas9 screen reveals a MYCN-amplified neuroblastoma dependency on EZH2. J. Clin. Invest. *128*, 446–462.

Choi, S.A., Kim, S.K., Lee, J.Y., Wang, K.C., Lee, C., and Phi, J.H. (2016). LIN28B is highly expressed in atypical teratoid/rhabdoid tumor (AT/RT) and suppressed through the restoration of SMARCB1. Cancer Cell Int. *16*, 32.

Cong, L., Ran, F.A., Cox, D., Lin, S., Barretto, R., Habib, N., Hsu, P.D., Wu, X., Jiang, W., Marraffini, L.A., and Zhang, F. (2013). Multiplex genome engineering using CRISPR/Cas systems. Science *339*, 819–823.

Deardorff, M.A., Bando, M., Nakato, R., Watrin, E., Itoh, T., Minamino, M., Saitoh, K., Komata, M., Katou, Y., Clark, D., et al. (2012). HDAC8 mutations in Cornelia de Lange syndrome affect the cohesin acetylation cycle. Nature *489*, 313–317.

Deisch, J., Raisanen, J., and Rakheja, D. (2011). Immunohistochemical expression of embryonic stem cell markers in malignant rhabdoid tumors. Pediatr. Dev. Pathol. *14*, 353–359.

Frühwald, M.C., Biegel, J.A., Bourdeaut, F., Roberts, C.W., and Chi, S.N. (2016). Atypical teratoid/rhabdoid tumors-current concepts, advances in biology, and potential future therapies. Neuro-oncol. *18*, 764–778.

Funato, K., Major, T., Lewis, P.W., Allis, C.D., and Tabar, V. (2014). Use of human embryonic stem cells to model pediatric gliomas with H3.3K27M histone mutation. Science *346*, 1529–1533.

Han, Z.Y., Richer, W., Fréneaux, P., Chauvin, C., Lucchesi, C., Guillemot, D., Grison, C., Lequin, D., Pierron, G., Masliah-Planchon, J., et al. (2016). The occurrence of intracranial rhabdoid tumours in mice depends on temporal control of Smarcb1 inactivation. Nat. Commun. *7*, 10421.

Hilden, J.M., Meerbaum, S., Burger, P., Finlay, J., Janss, A., Scheithauer, B.W., Walter, A.W., Rorke, L.B., and Biegel, J.A. (2004). Central nervous system atypical teratoid/rhabdoid tumor: results of therapy in children enrolled in a registry. J. Clin. Oncol. *22*, 2877–2884.

Hong, H., Takahashi, K., Ichisaka, T., Aoi, T., Kanagawa, O., Nakagawa, M., Okita, K., and Yamanaka, S. (2009). Suppression of induced pluripotent stem cell generation by the p53-p21 pathway. Nature *460*, 1132–1135.

Huang, W., Sherman, B.T., and Lempicki, R.A. (2009). Systematic and integrative analysis of large gene lists using DAVID bioinformatics resources. Nat. Protoc. *4*, 44–57.

Illingworth, R.S., Gruenewald-Schneider, U., Webb, S., Kerr, A.R., James, K.D., Turner, D.J., Smith, C., Harrison, D.J., Andrews, R., and Bird, A.P. (2010). Orphan CpG islands identify numerous conserved promoters in the mammalian genome. PLoS Genet. *6*, e1001134.

Johann, P.D., Erkek, S., Zapatka, M., Kerl, K., Buchhalter, I., Hovestadt, V., Jones, D.T.W., Sturm, D., Hermann, C., Segura Wang, M., et al. (2016). Atypical teratoid/rhabdoid tumors are comprised of three epigenetic subgroups with distinct enhancer landscapes. Cancer Cell *29*, 379–393.

Kim, J., Woo, A.J., Chu, J., Snow, J.W., Fujiwara, Y., Kim, C.G., Cantor, A.B., and Orkin, S.H. (2010). A Myc network accounts for similarities between embryonic stem and cancer cell transcription programs. Cell *143*, 313–324.

Kim, J., Hoffman, J.P., Alpaugh, R.K., Rhim, A.D., Reichert, M., Stanger, B.Z., Furth, E.E., Sepulveda, A.R., Yuan, C.X., Won, K.J., et al. (2013). An iPSC line from human pancreatic ductal adenocarcinoma undergoes early to invasive stages of pancreatic cancer progression. Cell Rep. *3*, 2088–2099.

Knutson, S.K., Warholic, N.M., Wigle, T.J., Klaus, C.R., Allain, C.J., Raimondi, A., Porter Scott, M., Chesworth, R., Moyer, M.P., Copeland, R.A., et al. (2013). Durable tumor regression in genetically altered malignant rhabdoid tumors by inhibition of methyltransferase EZH2. Proc. Natl. Acad. Sci. USA *110*, 7922–7927.

Langmead, B., and Salzberg, S.L. (2012). Fast gapped-read alignment with Bowtie 2. Nat. Methods *9*, 357–359.

Lee, D.R., Yoo, J.E., Lee, J.S., Park, S., Lee, J., Park, C.Y., Ji, E., Kim, H.S., Hwang, D.Y., Kim, D.S., and Kim, D.W. (2015). PSA-NCAM-negative neural crest cells emerging during neural induction of pluripotent stem cells cause mesodermal tumors and unwanted grafts. Stem Cell Reports *4*, 821–834.

Louis, D.N., Ohgaki, H., Wiestler, O.D., and Cavenee, W.K. (2016). WHO Classification of Tumours of the Central Nervous System, Fourth Edition (World Health Organization).

Martin, M. (2011). Cutadapt removes adapter sequences from high-throughput sequencing reads. EMBnet *17*, 10–12.

Ng, J.M., Martinez, D., Marsh, E.D., Zhang, Z., Rappaport, E., Santi, M., and Curran, T. (2015). Generation of a mouse model of atypical teratoid/rhabdoid tumor of the central nervous system through combined deletion of Snf5 and p53. Cancer Res. *75*, 4629–4639.

Oehme, I., Deubzer, H.E., Wegener, D., Pickert, D., Linke, J.P., Hero, B., Kopp-Schneider, A., Westermann, F., Ulrich, S.M., von Deimling, A., et al. (2009). Histone deacetylase 8 in neuroblastoma tumorigenesis. Clin Cancer Res. *15*, 91–99.

Ohnishi, K., Semi, K., Yamamoto, T., Shimizu, M., Tanaka, A., Mitsunaga, K., Okita, K., Osafune, K., Arioka, Y., Maeda, T., et al. (2014). Premature termination of reprogramming in vivo leads to cancer development through altered epigenetic regulation. Cell *156*, 663–677.

Poli, V., Fagnocchi, L., Fasciani, A., Cherubini, A., Mazzoleni, S., Ferrillo, S., Miluzio, A., Gaudioso, G., Vaira, V., Turdo, A., et al. (2018). MYC-driven epigenetic reprogramming favors the onset of tumorigenesis by inducing a stem cell-like state. Nat. Commun. *9*, 1024.

Rosenbloom, K.R., Armstrong, J., Barber, G.P., Casper, J., Clawson, H., Diekhans, M., Dreszer, T.R., Fujita, P.A., Guruvadoo, L., Haeussler, M., et al. (2015). The UCSC Genome Browser database: 2015 update. Nucleic Acids Res. *43*, D670–D681.

Sancho-Martinez, I., Nivet, E., Xia, Y., Hishida, T., Aguirre, A., Ocampo, A., Ma, L., Morey, R., Krause, M.N., Zembrzycki, A., et al. (2016). Establishment of human iPSC-based models for the study and targeting of glioma initiating cells. Nat. Commun. *7*, 10743.

Sanjana, N.E., Shalem, O., and Zhang, F. (2014). Improved vectors and genome-wide libraries for CRISPR screening. Nat. Methods *11*, 783–784.

Shibata, H., Komura, S., Yamada, Y., Sankoda, N., Tanaka, A., Ukai, T., Kabata, M., Sakurai, S., Kuze, B., Woltjen, K., et al. (2018). In vivo reprogramming drives Kras-induced cancer development. Nat. Commun. *9*, 2081.

Stricker, S.H., Feber, A., Engström, P.G., Carén, H., Kurian, K.M., Takashima, Y., Watts, C., Way, M., Dirks, P., Bertone, P., et al. (2013). Widespread resetting of DNA methylation in glioblastoma-initiating cells suppresses malignant cellular behavior in a lineage-dependent manner. Genes Dev. *27*, 654–669.

Subramanian, A., Tamayo, P., Mootha, V.K., Mukherjee, S., Ebert, B.L., Gillette, M.A., Paulovich, A., Pomeroy, S.L., Golub, T.R., Lander, E.S., and Mesirov, J.P. (2005). Gene set enrichment analysis: a knowledge-based approach for interpreting genome-wide expression profiles. Proc. Natl. Acad. Sci. USA *102*, 15545–15550.

Taguchi, J., and Yamada, Y. (2017). In vivo reprogramming for tissue regeneration and organismal rejuvenation. Curr. Opin. Genet. Dev. *46*, 132–140.

Takahashi, K., and Yamanaka, S. (2006). Induction of pluripotent stem cells from mouse embryonic and adult fibroblast cultures by defined factors. Cell *126*, 663–676.

Takahashi, K., Tanabe, K., Ohnuki, M., Narita, M., Ichisaka, T., Tomoda, K., and Yamanaka, S. (2007). Induction of pluripotent stem cells from adult human fibroblasts by defined factors. Cell *131*, 861–872.

Trapnell, C., Williams, B.A., Pertea, G., Mortazavi, A., Kwan, G., van Baren, M.J., Salzberg, S.L., Wold, B.J., and Pachter, L. (2010). Transcript assembly and quantification by RNA-Seq reveals unannotated transcripts and isoform switching during cell differentiation. Nat. Biotechnol. *28*, 511–515.

von Hoff, K., Hinkes, B., Dannenmann-Stern, E., von Bueren, A.O., Warmuth-Metz, M., Soerensen, N., Emser, A., Zwiener, I., Schlegel, P.G., Kuehl, J., et al. (2011). Frequency, risk-factors and survival of children with atypical teratoid rhabdoid tumors (AT/RT) of the CNS diagnosed between 1988 and 2004, and registered to the German HIT database. Pediatr. Blood Cancer *57*, 978–985.

Weingart, M.F., Roth, J.J., Hutt-Cabezas, M., Busse, T.M., Kaur, H., Price, A., Maynard, R., Rubens, J., Taylor, I., Mao, X.G., et al. (2015). Disrupting LIN28 in atypical teratoid rhabdoid tumors reveals the importance of the mitogen activated protein kinase pathway as a therapeutic target. Oncotarget *6*, 3165–3177.

Wilson, B.G., Wang, X., Shen, X., McKenna, E.S., Lemieux, M.E., Cho, Y.J., Koellhoffer, E.C., Pomeroy, S.L., Orkin, S.H., and Roberts, C.W. (2010). Epigenetic antagonism between polycomb and SWI/SNF complexes during oncogenic transformation. Cancer Cell *18*, 316–328.

Wong, D.J., Liu, H., Ridky, T.W., Cassarino, D., Segal, E., and Chang, H.Y. (2008). Module map of stem cell genes guides creation of epithelial cancer stem cells. Cell Stem Cell *2*, 333–344.

Yan, Y., Shin, S., Jha, B.S., Liu, Q., Sheng, J., Li, F., Zhan, M., Davis, J., Bharti, K., Zeng, X., et al. (2013). Efficient and rapid derivation of primitive neural stem cells and generation of brain subtype neurons from human pluripotent stem cells. Stem Cells Transl. Med. *2*, 862–870.

Yong, K.J., Gao, C., Lim, J.S., Yan, B., Yang, H., Dimitrov, T., Kawasaki, A., Ong, C.W., Wong, K.F., Lee, S., et al. (2013). Oncofetal gene SALL4 in aggressive hepatocellular carcinoma. N. Engl. J. Med. *368*, 2266–2276.

STAR★METHODS

KEY RESOURCES TABLE

REAGENT or RESOURCE	SOURCE	IDENTIFIER
Antibodies		
Anti-SALL4	Abnova	Cat# clone 6E3; RRID: AB_566160
Anti-LIN28A	Cell Signaling Technology	Cat# 8706; RRID: AB_10896850
Anti-LIN28B	Cell Signaling Technology	Cat# 5422; RRID: AB_10697489
Anti-Ki67 (SP6)	Abcam	Cat# ab16667; RRID: AB_302459
Anti-INI1/SNF5	Sigma-Aldrich	Cat# SAB4200202; RRID: AB_10697389
Anti-Vimentin (V9)	SantaCruz	Cat# sc-6260; RRID: AB_628437
Anti-GFAP	DAKO	Cat# IR524
Anti-CD99	DAKO	Cat# clone 12E7; RRID: AB_2076419
Anti-S100	DAKO	Cat# GA504
Anti-EMA	Novocastra	Cat# NCL-L-EMA; RRID: AB_563531
Anti-SMA	Nichirei	Cat# clone1A4
Anti-Synaptophysin	Nichirei	Cat# clone27G12
Anti-NESTIN	Millopore	Cat# MAB5326; RRID: AB_2251134
Anti-TP53	Santa Cruz	Cat# sc-126; RRID: AB_628082
Anti-β-actin	Santa Cruz	Cat# sc-47778; RRID: AB_626632
ECL anti-mouse IgG, HRP-linked whole antibody from sheep	GE Healthcare	Cat# NA931; RRID: AB_772210
ESC anti-rabbit IgG and HRP-linked whole antibody from donkey	GE Healthcare	Cat# NA934; RRID: AB_772206
Anti-PSA-NCAM antibody conjugated with microbeads	Miltenyi Biotec	Cat# 130-92-981
Anti-PSA-NCAM	Millipore	Cat# MAB5324; RRID: AB_95211
StemFit AK03N	Ajinomoto	Cat# AK03N
StemFit AK02N	Ajinomoto	Cat# AK02N
Laminin-511	Wako	Cat# 892012
PSC Neural Induction Medium	Life Technologies	Cat# A1647801
Y27632	Wako	Cat# 253-00513
Chemicals, Peptides, and Recombinant Proteins		
GSK126	Funakoshi	Cat# A-1275
PCI34051	Selleck	Cat# S2012
siGENOME SMARTpool siRNA, RAD21	Dharmacon	Cat# M-006832-01-0005
siGENOME SMARTpool siRNA, Non-Targeting	Dharmacon	Cat# D-001206-13-05
Critical Commercial Assays		
AlamarBlue cell viability reagent	Bio-Rad	Cat# BOF012B
Cell Counting Kit-8	Dojindo	Cat# 341-07761
Human Gene 1.0 ST Array	Affymetrix	Cat# 901086
Truseq Stranded mRNA LT sample prep kit	Illumina	Cat# RS-122-2101, RS-122-2102
Deposited Data		
Microarray data	This paper	GSE118653
RNA-seq data	This paper	GSE118654
Affymetrix Human Gene 1.0ST Array datasets	Gene Expression Omnibus	GEO: GSE26313, GSE45265, GSE36947, GSE18296 and GSE27667

(*Continued on next page*)

Continued

REAGENT or RESOURCE	SOURCE	IDENTIFIER
Affymetrix Human Genome U133 Plus 2.0 Array datasets	Gene Expression Omnibus	GEO: GSE70678, GSE37418, GSE53733, GSE16476, GSE11151, GSE53224, GSE75271, GSE10927, GSE66272, GSE62232, GSE73038 and GSE22392
Illumina HumanMethylation450 BeadChip datasets	Gene Expression Omnibus	GEO: GSE60821, GSE92462, GSE70460, GSE75153, GSE36278 and GSE73801
Experimental Models: Cell Lines		
Human: 201B7 hiPSC	Laboratory of Masato Nakagawa	hiPS Cell Line: 201B7
Human: 1383D6 hiPSC	Laboratory of Masato Nakagawa	hiPS Cell Line: 1383D6
Human: KUP-ATRT-1	Kyoto University	N/A
Human: A204	ATCC	HTB-82
Human: G401	ATCC	CRL-1441
Human: G402	ATCC	CRL-1440
Human: SK-N-AS	ATCC	CRL-2137
Human: SK-N-BE(2)	ATCC	CRL-2271
Human:T98G	Cell Resource Center for Biomedical Research, Institute of Development Aging and Cancer, Tohoku University	TKG0471
Human:A172	Cell Resource Center for Biomedical Research, Institute of Development, Aging and Cancer, Tohoku University	TKG0183
Human:U87-MG	ATCC	HTB-14
Experimental Models: Organisms/Strains		
Mouse: NOD/ShiJic-*scid*Jcl	CLEA Japan	N/A
Oligonucleotides		
Oligos for sgRNA, see Table S1	This study and Brunello Library	Human CRISPR Knockout Pooled Library (Brunello)
Primers for quantitative PCR, see Table S4	This study	N/A
Oligos for TP53 sgRNA: CGCTATCTGAGCAGCGCTCA	This study	N/A
Oligos for SMARCB1 sgRNA: TGAGAACGCATCTCAGCCCG	This study	N/A
Recombinant DNA		
lentiCRISPR v2	Sanjana et al., 2014	Addgene: #52961
pX330-U6-Chimeric BB-CBh-hSpCas9	Cong et al., 2013	Addgene: #42230
pMYs-IRES-GFP	Cell Biolads	Cat# RTV-021
pMYs-c-MYC-IRES-GFP	This study	N/A
pMx-GFP	Cell Biolads	Cat# VPK-302
pMxs-hOCT4	Takahashi et al., 2007	Addgene: #17217
pMxs-hSOX2	Takahashi et al., 2007	Addgene: #17218
pMxs-hKLF4	Takahashi et al., 2007	Addgene: #17219
pMXs-hc-MYC	Takahashi et al., 2007	Addgene: #17220
pCMV-VSV-G	Cell Biolads	Cat# VPK-302
pMD2.G	Addgene	Cat# 12259
psPAX2	Addgene	Cat# 12260
Software and Algorithms		
GSEA software (version 3.0)	Subramanian et al., 2005	http://software.broadinstitute.org/gsea/index.jsp
DAVID bioinformatics database website	Huang et al., 2009	https://david.ncifcrf.gov/home.jsp

Continued		
REAGENT or RESOURCE	SOURCE	IDENTIFIER
Graphpad Prism 6	MDF	http://www2.usaco.co.jp/shop/c/cGPPrism/
GeneSpring GX software (version 12)	Agilent Technology	https://www.chem-agilent.com/contents.php?id=27881
Other		
Gene set: WONG_EMBRYONIC_STEM_CELL_CORE	Wong et al., 2008	http://software.broadinstitute.org/gsea/msigdb/cards/WONG_EMBRYONIC_STEM_CELL_CORE
Gene set: hESC-like module	Wong et al., 2008	Table S5
Gene set: Core Human module	Kim et al., 2010	Table S3

CONTACT FOR REAGENT AND RESOURCE SHARING

Further information and requests for resources and reagents should be directed to and will be fulfilled by the Lead Contact, Yasuhiro Yamada (yasu@ims.u-tokyo.ac.jp).

EXPERIMENTAL MODEL AND SUBJECT DETAILS

Mice
All animal experiments were approved by the Animal Experiment Committee at CiRA and IMSUT, and the care of the animals was in accordance with institutional guidelines. All mice used for the present study were on NOD/ShiJic-*scid*Jcl (NOD SCID) mice of both sexes (8-10 weeks). NOD SCID mice were purchased from CLEA Japan, Inc. Mice were kept in the animal facility with 12 hours of light and dark cycle with food and water *ad libitum*.

Cell culture and neural induction
201B7 and 1383D6 hiPSCs (provided by Masato Nakagawa, CiRA) were cultured in StemFit AK03N or AK02N (Ajinomoto) on cell culture plates coated with laminin-511 (Wako) at $37°C$ with 5% CO_2. For neural induction, culture medium was switched to GIBCO PSC Neural Induction Medium (Life Technologies) containing Neurobasal medium and GIBCO PSC neural induction supplement. At day 7 of the neural induction, these cells were dissociated and plated in neural expansion medium containing 50% Neurobasal medium, 50% Advanced DMEM/F12 and neural induction supplement. Cells were treated with 10 μM ROCK inhibitor Y27632 (Wako) at the time of plating overnight to prevent cell death. To further induce differentiation, culture medium was switched to Neurobasal medium containing 2% B-27 Supplement (GIBCO) and GlutaMAX Supplement (GIBCO).

KUP-ATRT-1, an AT/RT cell line, was established at Kyoto University. Other tumor cell lines were purchased from ATCC or Cell Resource Center for Biomedical Research, Institute of Development, Aging and Cancer, Tohoku University. Tumor cells were cultured with RPMI 1640 (GIBCO) or MEM, GlutaMAX^{TM} supplement (GIBCO) containing 10% fetal bovine serum (FBS) at $37°C$ with 5% CO_2.

Establishment of hiPSC $^{SMARCB1-/-;\ TP53-/-}$ -derived cancer cell line
A block of hiPSC $^{SMARCB1-/-;\ TP53-/-}$-derived tumor was mechanically minced. The minced tissue was digested with StemPro Accutase Cell Dissociation Reagent (GIBCO) at $37°C$ for 15 minutes. After washing, the tissue was triturated and passed through a 100 μm cell strainer. Cells were plated onto cell culture plates coated with laminin-511 in AK03N media. Passaging of the cultures was performed approximately once a week.

METHOD DETAILS

TP53 and SMARCB1 knockout using CRISPR/Cas9 system
The *TP53* and *SMARCB1* genes were knocked-out with P3 primary cell 4D-Nucleofector X Kit (Lonza). 201B7 cells were transfected with modified pX330-U6-Chimeric_BB-CBh-hSpCas9 plasmid (Addgene: Plasmid #42230) (Cong et al., 2013) expressing a sgRNA against *TP53* (CGCTATCTGAGCAGCGCTCA) or *SMARCB1* (TGAGAACGCATCTCAGCCCG) with puromycin-resistance gene. To avoid genomic integration, puromycin selection (1 μl/ml) was performed only for two days. Each single colony was picked-up and expanded. The knockout for TP53 and SMARCB1 was confirmed by sequencing and western blot.

Retroviral transduction
To generate retroviral vectors, Plat-GP cells on 150 mm dishes were cultured with DMEM containing 100 U/ml penicillin, 100 μ g/ml streptomycin (P/S) (Nacalai tesque) and 10% FBS (GIBCO) until 70%–80% confluency and were transfected with 12.375 μg retroviral

vector plasmid (pMx-GFP, pMxs-hOCT4, pMxs-hSOX2, pMxs-hKLF4, pMxs-hc-MYC and pMYs-IRES-GFP or pMYs-hc-MYC-IRES-GFP) (Addgene, Cell Biolabs, Inc.) (Takahashi et al., 2007) independently in combination with 5.625 μg pCMV-VSV-G (Cell Biolabs, Inc.) using Lipofectamin 2000 (Life technologies). 24 hours after the transfection, the culture media was refreshed, and the supernatant was collected over 3 consecutive days. The filtered supernatant was concentrated by PEG-*it* (System Biosciences), re-suspended, aliquoted and stored at −80°C. 1×10^6 of NPLCs$^{SMARCB1-/-;\ TP53-/-}$ or PSA-NCAM-positive NPLCs$^{TP53-/-;\ SMARCB1-/-}$ were incubated with the concentrated virus-containing supernatant overnight. Five days after the infection, cells were harvested and transplanted into the mouse brain. At the same time, RNA was extracted from the infected cells.

Xenograft tumor model
1 μl of 4×10^5 cells were injected into the left striatum of NOD SCID mice at the coordinates of 1.5 mm lateral from the bregma and 2 mm deep from the dura using a 10 μl Hamilton syringe with a flow rate of 1 μl per minute. MRI studies were performed on a 1.5-Tesla MRI scanner (MRmini SA1508; DS Pharma Biomedical). Transplanted mice were traced until they died or showed some neurological signs (observation period: 4-31weeks).

Histological analysis and immunostaining
Mice were transcardially perfused with 1 × PBS followed by 4% paraformaldehyde. Following dissection, brain tissues were transferred to PBS and subsequently embedded in paraffin and sectioned. Sections were stained with hematoxylin and eosin (H&E), and serial sections were used for the immunohistochemical analysis. The primary antibodies, which were incubated at 4°C overnight in blocking buffer, were as follows: anti-SALL4 (Abnova: #clone 6E3), anti-LIN28A (Cell Signaling Technology: #8706), anti-LIN28B (Cell Signaling Technology: #5422), anti-Ki67 (SP6) (Abcam: #ab16667), anti-INI1/SNF5 (Sigma-Aldrich: #91735), anti-Vimentin (V9) (SantaCruz: #sc-6260), anti-GFAP (DAKO: #IR524), anti-CD99 (DAKO: #clone 12E7), anti-S100 (DAKO: #GA504), anti-EMA (Novocastra: #NCL-L-EMA), anti-SMA (Nichirei: #clone1A4) and anti-Synaptophysin (Nichirei: #clone27G12). The sections were incubated with the appropriate species of HRP-conjugated secondary antibodies (Nichirei, Histofine) at room temperature for 30 minutes, and chromogen development was performed using DAB (Nichirei). The stained slides were counterstained with Meyer hematoxylin. The histopathological sections were reviewed by two different pathologists (Yo Y and Ya Y) who have been certified by the Japanese Society of Pathology.

Immunofluorescent staining
The samples were fixed with 4% paraformaldehyde for five minutes and soaked in PBS. They were then incubated with anti-NESTIN (Millipore: #MAB5326) at 4°C overnight in blocking buffer and were processed with × 500 DAPI (Invitrogen) and × 150 fluorescence-labeled secondary antibodies diluted with 0.5% BSA in PBS for 90 minutes at room temperature. After washing in PBS for 5 minutes twice, the samples were mounted and evaluated with a confocal laser-scanning microscope (Zeiss LSM700 or 710).

Western blot analysis
Cell lysates were prepared in RIPA buffer with protease inhibitors. Protein samples were carried out according to standard methods. The primary antibodies used were anti-INI1/SNF5 (Sigma-Aldrich: #91735), anti-TP53 (Santa Cruz Biotechnology: #sc-126) and anti-β-actin (Santa Cruz, sc-47778). The secondary antibodies used were ECL anti-mouse IgG, HRP-linked whole antibody from sheep (NA931, GE Healthcare), ECL anti-rabbit IgG and HRP-linked whole antibody from donkey (NA934, GE Healthcare). ImageQuant LAS4000 (GE Healthcare) was used for band detection.

Magnetic-based cell sorting (MACS) and flow cytometric analysis
Expanded NPLCs$^{SMARCB1-/-;\ TP53-/-}$ were exposed to 10 μM of Y27632 (Wako) for more than one hour to prevent cell death prior to the MACS procedure. After dissociation, the cells were briefly blocked in 0.5% BSA-PBS solution and then incubated with anti-PSA-NCAM antibody conjugated with microbeads (Miltenyi Biotec: #130-92-981) for 15 minutes at 4°C. After extensive washing, the cell suspension was loaded on a separation column (LS column) that was attached to a magnetic stand. Positively-labeled cells that remained in the column were eluted to a tube with culture medium for further manipulation and analysis. After magnetic cell separation, we further used flow cytometry to examine the purity of PSA-NCAM-positive cells. MACS-sorted cells were cultured for 24 hours and stained with anti-PSA-NCAM antibody (Millipore: #MAB5324) for 15 minutes at 4°C followed by CF488-conjugated secondary antibody for 10 minutes at 4°C. The positive fraction was evaluated by flow cytometry (Aria II, BD) using non-stained cells as a control.

Genetic screening with lentiviral CRISPR/Cas9 system
We utilized the lentiCRISPR v2 (Addgene #52961) (Sanjana et al., 2014) for one-by-one gene disruption. The candidate genes were selected based on the previous literatures and databases (Table S1). The lentiviral vector has both a sgRNA scaffold and a Cas9 to induce insertions and deletions (indels) at the genomic locus of the cells into which they are transduced.

The lentiviral cloning and production were performed as described previously (Sanjana et al., 2014). Briefly, the complementary oligonucleotides for sgRNAs (Table S1) were annealed by heating to 95°C for 3 minutes and subsequent cooling to 60°C for 3 minutes on ice. The lentiCRISPR v2 plasmid was digested with BsmBI (New England Biolabs) at 55°C overnight and purified by FastGene

Gel/PCR Extraction Kit (Genetics). The annealed oligonucleotides were ligated into the digested lentiCRISPR v2 plasmid by Ligation high Ver.2 (TOYOBO) at 16°C for 30 minutes. The reactants were transformed into Stbl3 chemically competent *E. coli* (Thermo Fisher Scientific). The grown colonies were analyzed by Sanger sequencing with ABI 3500xL (Applied Biosystems) to confirm correctly recombined clones. The lentiviral plasmids were extracted by GenElute Plasmid Miniprep Kit (Sigma).

To generate lentiviral vectors, HEK293T cells on 60 mm dishes were cultured with DMEM containing 100 U/ml penicillin, 100 μg/ml streptomycin (P/S) (Nacalai tesque), 10% FBS (GIBCO) until 70%–80% confluency and transfected with 2.4 μg lenti-CRISPR v2 plasmid, 0.8 μg pMD2.G (Addgene #12259) and 1.6 μg psPAX2 (Addgene #12260) using PEI max (Polysciences). 24 hours after transfection, culture media were refreshed, and the supernatant was collected over 3 consecutive days. The filtered supernatant was concentrated by PEG-*it* (System Biosciences), re-suspended, aliquoted and stored at −80°C. No lentiviral functional titration was performed. Instead, we measured base-line cell viability at days 3-5 during the screening process to adjust the transduction efficiency bias as explained below. The screening was performed with 96-well plate format in duplicate. Each cell line was plated to be 70%–80% confluent at the day of lentiviral transduction (day 0). We avoided using outer lanes, where the value could be variable because of the media evaporation. At day 0, virus-containing supernatant was added to each well, and 24 hours later, puromycin was added to eliminate non-transfected cells. At days 3-5, the baseline cell viability was assessed using alamarBlue (Bio-Rad). Fluorescence was detected with 2104 EnVision Multi Detection Microplate Reader (Perkin Elmer). The average fluorescence intensity value in blank wells was subtracted to determine the fluorescence intensity value of each well. Media were replaced every 2-3 days. When wells transduced with non-targeting control (NTC) sgRNA reached 70%–80% confluency, cell viability was measured again by alamarBlue to assess the effect of each knockout on cell growth. Cell growth rates were calculated as follows: the average of duplicate fluorescence intensity values was divided by the average at baseline. Cell growth rates were compared with NTC sgRNA-transduced cells.

To confirm the CRISPR/Cas9-mediated cleavage efficiency in this screening, we randomly selected 20 genes among the candidate genes and assessed the indel frequency at days 3 and 7 in the SK-N-BE(2) cell line. The indel frequency was calculated by TIDE software (https://tide.nki.nl) (Brinkman et al., 2014). The TIDE software parameters used in this study were as follows: left boundary, 100 bp; right boundary, −10 bp; decomposition window, 115-685 bp; indel size range, 20 bp.

The titration of puromycin was pre-determined for each cell line to efficiently eliminate non-transduced cells at days 3-5. The concentrations of puromycin used in this study were 1.0, 1.0 and 1.5 μg/ml for hiPSC $^{SMARCB1−/−; TP53−/−}$-derived cancer cell line, SK-N-BE(2) and SK-N-AS, respectively.

Cell growth inhibition assays and cell proliferation assays

In vitro drug sensitivity was determined using alamarBlue cell viability reagent (Bio-Rad) according to the manufacturer's protocol. Cells were plated into 96-well culture plates at a density of 2×10^3 cells/well. Cells were treated with 10 μM of DMSO, GSK126, PCI34051 or a combination of GSK126 and PCI34051 at day 0 and incubated for 7 days. The experiment was performed in triplicate, and each sample was measured three times. Fluorescence intensity was detected with 2104 EnVision Multi Detection Microplate Reader. The average fluorescence intensity value of blank wells was subtracted to determine the fluorescence intensity of each well at each time point. The average fluorescence intensity of DMSO-treated cells at day 7 was set to 1. Cell Counting Kit-8 (Dojindo) was also used to examine *in vitro* cell proliferation. Abosrbance was measured using iMark Microplate Absorbance Reader (Bio-Rad).

siRNA transfection

siRNA transfection was performed using Lipofectamine RNAi Max (Invitrogen). We performed knockdown assays with a siRNA targeting *RAD21* (Dharmacon). Nontargeting siRNA (Dharmacon) was used as a control. Culture medium was exchanged every 2 days, and cell proliferation was determined using Cell Counting Kit-8 (Dojindo).

RNA Preparation, qRT-PCR and microarray analysis

Total RNA was isolated using the RNeasy Plus Mini kit (QIAGEN). The qRT-PCR analysis was performed using GoTaq qPCR Master Mix (Promege). The specific primer pairs used for amplification are shown in Table S4. The transcript levels were normalized to the *GAPDH* level. The microarray analysis was performed using Human Gene 1.0 ST Array (Affymetrix) in accordance with the manufacturer's instructions, GeneSpring GX software program (version 12; Agilent Technology), GSEA software (version 3.0) and the DAVID bioinformatics database website (https://david.ncifcrf.gov/home.jsp). The gene sets of the hESC-like module (Wong et al., 2008) and the Core Human module (Kim et al., 2010) were used for the clustering analysis. The gene set of "WONG_EMBRYONIC_STEM_CELL_CORE" in MSigDB (version 6.0) was used for the GSEA analysis.

Library preparation for RNA sequencing

200 ng of total RNA was prepared for the library construction. High-quality RNA (RNA Integrity Number value $\geq$ 7) assessed by Bioanalyzer was used for the library preparation. RNA-seq libraries were generated using the Truseq Stranded mRNA LT sample prep kit (Illumina). PolyA-containing mRNA was purified by poly-T oligo-attached magnetic beads, and the RNA was fragmented and primed for cDNA synthesis. Cleaved RNA fragments were reverse transcribed into first strand cDNA using transcriptase and random primers. Second strand cDNA was synthesized by the incorporation of dUTP, and ds cDNA was separated using AMPure XP beads (BECKMAN COULTER). A single 'A' nucleotide was added to the 3′ ends of the blunt fragments, and then adapters with

index were ligated to the ends of the ds cDNA. ds cDNA fragments were amplified by PCR with PCR primer Cocktail. The number of PCR cycles was minimized (15 cycles) to avoid skewing the representation of the libraries. RNA-seq libraries were sequenced on NextSeq 500 (75 bp or 86 bp single, Illumina).

RNA-seq data analyses

The sequenced reads were mapped to the human reference genome (hg38) using Tophat2 (version 2.1.1) with the GENCODE (version 27) annotation gtf file and the aligner Bowtie2-2.3.4 (Langmead and Salzberg, 2012) after trimming adaptor sequences and low-quality bases by cutadapt-1.16 (Martin, 2011). The uniquely mapped reads were used for further analyses. Using cufflinks-2.2.1 (Trapnell et al., 2010) with the human GENCODE (version 27, protein coding) annotation gtf file, reads per kilobase of exon per million mapped reads (RPKM) were calculated as the expression levels of each gene. RPKM values were used for the GSEA method.

DNA methylation analyses for infinium methylation array data

Infinium450K data were obtained from GSE60821 (hESC), GSE92462 (hESC, NSCs, normal brain and fetal brain), GSE36278 (normal brain, fetal brain and GBM), GSE75153 (MB), GSE73801 (ETMR) and GSE70460 (AT/RT). Previously described human CGIs (Illingworth et al., 2010) were used for the methylation analysis. The UCSC LiftOver tools (http://genome.ucsc.edu/) (Rosenbloom et al., 2015) were used to convert the coordinates of hg18 assembly into those of hg19 assembly. After the conversion of the CGI regions, overlap regions were merged into a single region. The UCSC refGene table was used to determine the TSS sites. The median signal value of the probes within each CGI and TSS $\pm$ 1,500 bp was calculated as the methylation signal of the region. Brain-methylated regions and brain-unmethylated regions were defined as the CGI and TSS $\pm$ 1,500 bp that represent higher (> 0.6) and lower (< 0.6) brain-methylation (median methylation signals in 7 brain samples), respectively, compared to PSC-methylation (median methylation signals in 6 PSC samples). The all probe methylation signals within the indicated regions were used in violin plots.

Quantification and Statistical Analysis

To quantify the dominance of rhabdoid cells in tumors, an H&E stained section was randomly photographed at 10 × magnification. Three or 4 pictures for each sample were processed with ImageJ software (NIH) to evaluate the positive area of rhabdoid cells. The positive area was determined by the area of rhabdoid cells divided by the area of the tumor in the histological image. To assess *SALL4*-positive cells, each section was randomly photographed at 200 × magnification. Positive nuclei in tumor cells were counted using five images. The number of positive nucleus was divided by the number of total nuclei of tumor cells in each image. These results were evaluated with Graphpad Prism 6 software.

All values and graphs are expressed as the mean with 95% confidence interval or the median with interquartile range, and statistical analyses were performed using unpaired t test with Welch's correction or Mann-Whitney U test for continuous variables and Fisher's exact test for categorical variables. One-way ANOVA or Kruskal-Wallis test was performed to compare multiple groups. Dunnett's or Dunn's multiple comparisons test was used for multiple comparisons. Kaplan-Meier survival curves were compared using the log-rank test. Statistical parameters including statistical significance and *n* values are described in the figures and figure legends. A value of $p < 0.05$ was considered significant. All analyses were conducted using Graphpad Prism 6 software.

DATA AND SOFTWARE AVAILABILITY

All data analyzed by microarray and RNA-seq have been deposited in the Gene Expression Omnibus (GEO) under accession numbers GSE118653 and GSE118654.

Supplemental Information

Human Pluripotent Stem Cell-Derived Tumor Model

Uncovers the Embryonic Stem Cell Signature as a

Key Driver in Atypical Teratoid/Rhabdoid Tumor

Yukinori Terada, Norihide Jo, Yoshiki Arakawa, Megumi Sakakura, Yosuke Yamada, Tomoyo Ukai, Mio Kabata, Kanae Mitsunaga, Yohei Mineharu, Sho Ohta, Masato Nakagawa, Susumu Miyamoto, Takuya Yamamoto, and Yasuhiro Yamada

Supplemental Information

Human pluripotent stem cell-derived tumor model uncovers the embryonic stem cell signature as a key driver in atypical teratoid/rhabdoid tumor

Yukinori Terada, Norihide Jo, Yoshiki Arakawa, Megumi Sakakura, Yosuke Yamada, Tomoyo Ukai, Mio Kabata, Kanae Mitsunaga, Yohei Mineharu, Sho Ohta, Masato Nakagawa, Susumu Miyamoto, Takuya Yamamoto, Yasuhiro Yamada

Figure S1: Generation of an atypical teratoid/rhabdoid tumor model using hiPSCs lacking *SMARCB1*, related to Figure 1

Figure S1: Generation of an atypical teratoid/rhabdoid tumor model using hiPSCs lacking *SMARCB1*, related to Figure 1

(A) A qRT-PCR for pluripotency genes and neural differentiation genes. Data are presented as the mean ± SD of biological triplicates. The mean expression level of hiPSCs [201B7] or NPLCs [201B7] was set to 1.

(B) A qRT-PCR for neuronal differentiation genes after the neuronal differentiation of NPLCs for 7 days. Data are presented as the mean ± SD of biological triplicates. The mean expression level of NPLCs (differentiation 7 days) was set to 1.

(C) Gene ontology enrichment analysis of NPLCs [SMARCB1-/-; TP53-/-] compared to undifferentiated hiPSCs [SMARCB1-/-; TP53-/-]. Analysis was performed using DAVID (Huang da et al., 2009). Genes showing ≥ 2-fold changes in NPLCs [SMARCB1-/-; TP53-/-] compared to hiPSCs [TP53-/-; SMARCB1-/-] were used in the analysis.

(D) Cell proliferation assays of hiPSCs and NPLCs. **$p<0.01$, ***$p<0.001$ (One-way ANOVA and Dunnett's multiple comparisons test).

(E) Macroscopic tumor incidence after xenograft transplantation of hiPSCs and NPLCs into the brain of immunocompromised mice.

(F) Microscopic tumor incidence after xenograft transplantation of hiPSCs and NPLCs into the brain of immunocompromised mice.

(G) Representative histological images of microscopic tumors. The iPSC [201B7]-derived tumor exhibits a teratoma-like histology, which contains ciliated epithelial cells (left), while the NPLCs [TP53-/-]-tumor shows a scar-like histology (right). Scale bars, 500 μm (top) and 50 μm (bottom).

(H) Western blot analysis of 1383D6 iPSCs [SMARCB1-/-] for SMARCB1 and β-actin shows the lack of SMARCB1 in 1383D6 iPSCs [SMARCB1-/-].

(I) Representative histological images of a 1383D6 iPSC [SMARCB1-/-]-derived tumor and 1383D6 NPLC [SMARCB1-/-]-derived tumor. Note that the 1383D6 iPSC [SMARCB1-/-]-derived tumor contains rhabdoid cells. Scale bars, 500 μm (top) and 20 μm (bottom).

(J) Quantification of the rhabdoid area within 1383D6 iPSC [SMARCB1-/-]-derived tumors and 1383D6 NPLC [SMARCB1-/-]-derived tumors. Data are represented as the median with interquartile range. *$p<0.05$ (Mann-Whitney U test).
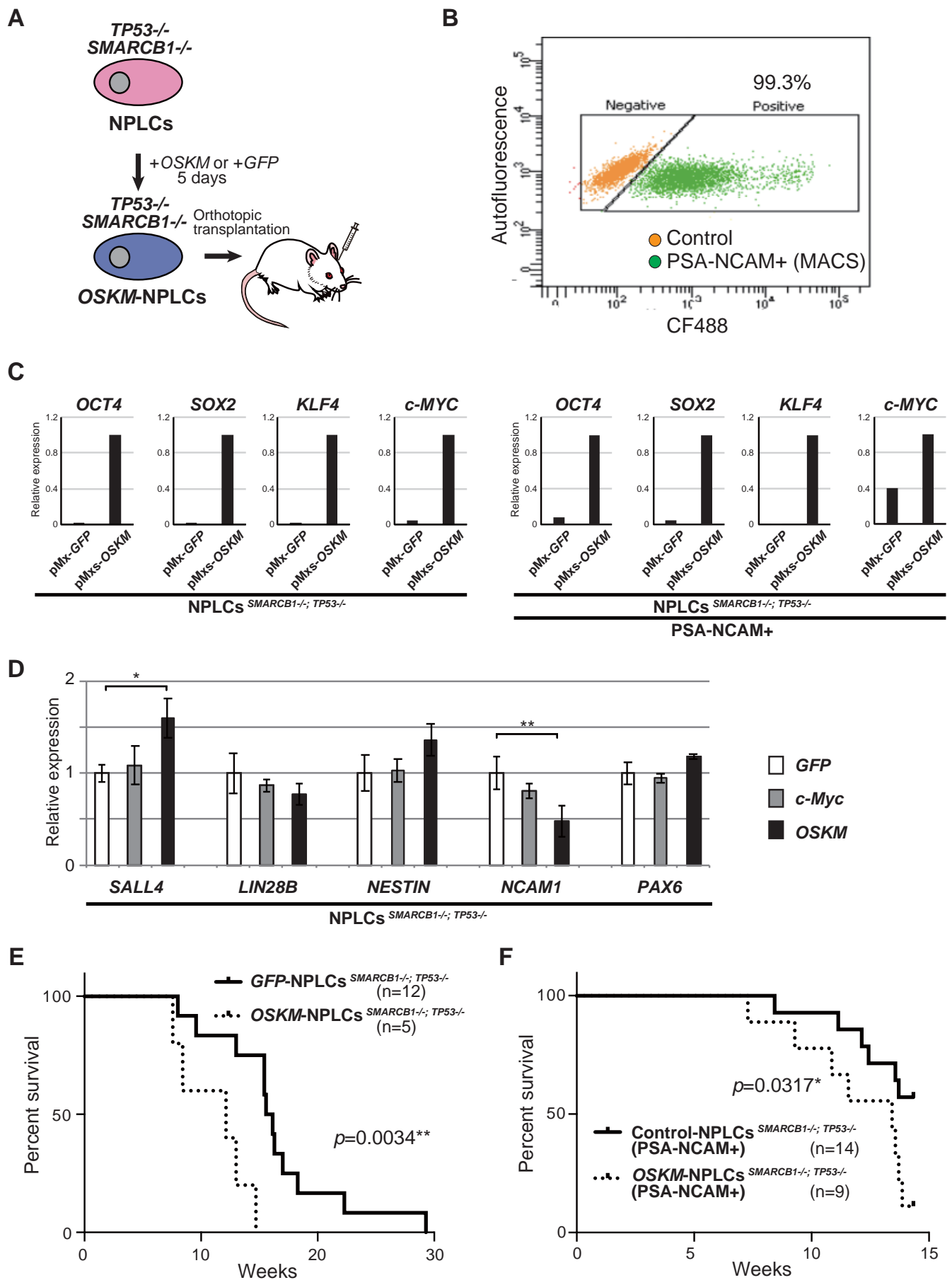
Figure S2: Induction of the ESC-like signature leads to rhabdoid phenotype in tumors, related to Figure 2

Figure S2: Induction of the ESC-like signature leads to rhabdoid phenotype in tumors, related to Figure 2

(A) A schematic illustration of a xenograft transplantation study of NPLCs $^{SMARCB1-/-; TP53-/-}$ transduced with *GFP* (*GFP*-NPLCs) or four reprogramming factors (*OCT4, SOX2, KLF4* and *c-MYC*) (*OSKM*-NPLCs).

(B) A flow cytometric analysis of PSA-NCAM expression in NPLCs $^{SMARCB1-/-; TP53-/-}$ after sorting with PSA-NCAM antibody by magnetic activated cell sorting (MACS).

(C) A qRT-PCR for *OCT4, SOX2, KLF4* and *c-MYC* at 5 days after the transduction of *GFP* or *OSKM* in NPLCs $^{SMARCB1-/-; TP53-/-}$. Data are presented as the mean of technical triplicates. The mean expression level of *OSKM*-NPLCs was set to 1.

(D) A qRT-PCR for pluripotent genes and neural differentiation genes at 5 days after the transduction of *GFP, c-MYC* or *OSKM* in NPLCs $^{SMARCB1-/-; TP53-/-}$ *in vitro*. Data are presented as the mean of three biological replicates with standard deviation. The mean expression level of *GFP*-NPLCs was set to 1. *$p<0.05$, **$p<0.01$ (One-way ANOVA and Dunnett's multiple comparisons test).

(E) (F) Survival curve of mice transplanted with *GFP*-NPLCs or *OSKM*-NPLCs. Note that mice inoculated with *OSKM*-NPLCs exhibit poor survival when compared to mice inoculated with control NPLCs. Kaplan-Meier analysis was performed. *$p<0.05$, **$p<0.01$ (Log-rank test).
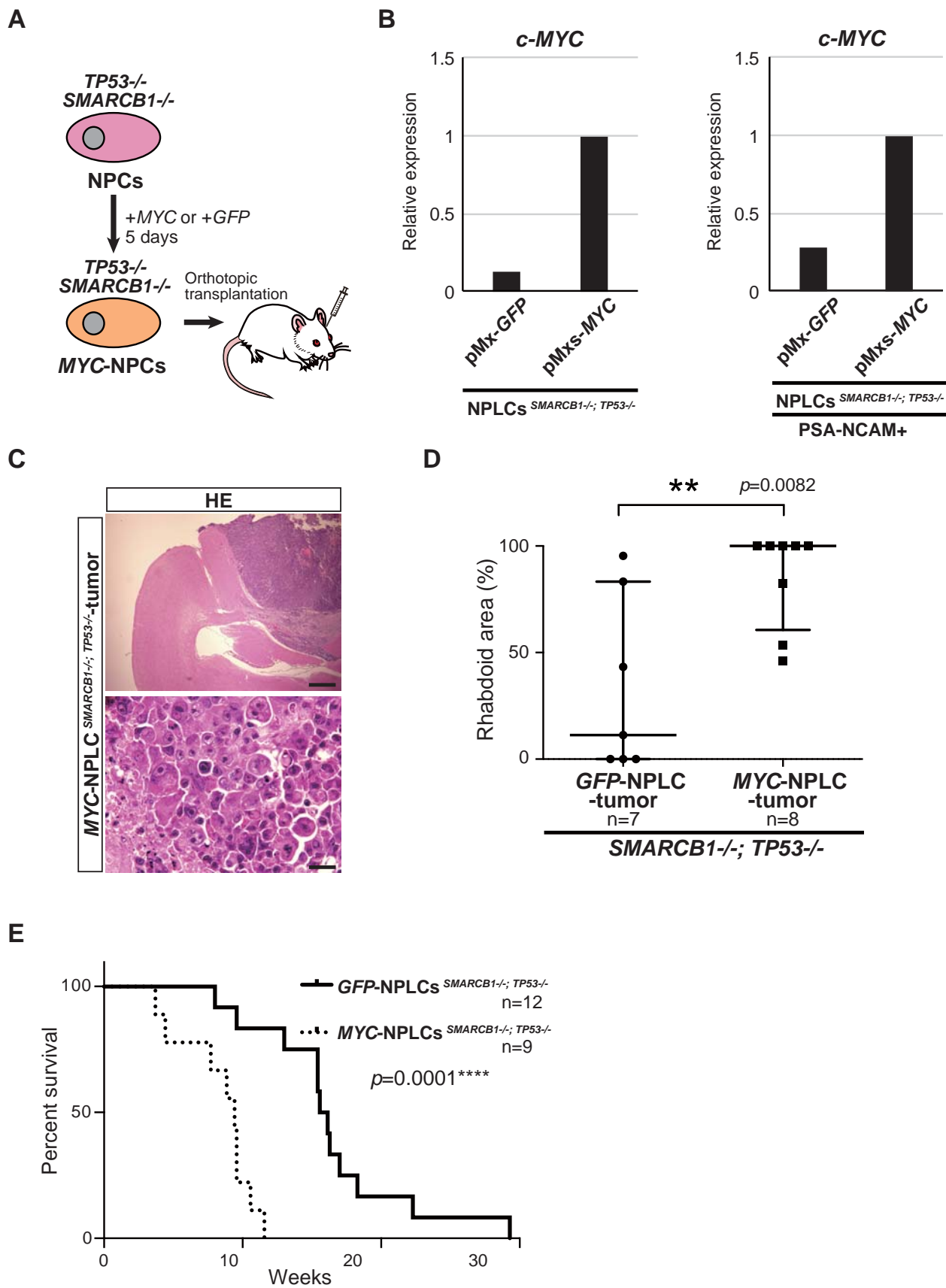
Figure S3: *c-MYC* **induces activation of the ESC-like signature and drives rhabdoid tumors** *in vivo*, **related to Figure 3**

Figure S3: *c-MYC* induces activation of the ESC-like signature and drives rhabdoid tumors *in vivo*, related to Figure 3

(A) A schematic illustration of a xenograft transplantation study of NPLCs $^{SMARCB1-/-; TP53-/-}$ transduced with *GFP* (*GFP*-NPLCs) or *c-MYC* (*MYC*-NPLCs). Control *GFP*-NPLCs are the same as Figure S2.

(B) A qRT-PCR for *c-MYC* after the transduction of *GFP* or *c-MYC* in NPLCs $^{SMARCB1-/-; TP53-/-}$. Data are presented as the mean of technical triplicates. The mean expression level of *MYC*-NPLCs was set to 1.

(C) Representative histological images of a *MYC*-NPLC-derived tumor. Note that a number of rhabdoid cells are observed in the tumor. Scale bars, 500 μm (upper) and 20 μm (lower).

(D) Quantification of the rhabdoid area in *GFP*-NPLC- and *MYC*-NPLC-derived tumors. Data are represented as the median with interquartile range. **$p<0.01$ (Mann-Whitney U test).

(E) Survival curves of mice transplanted with *GFP*-NPLCs or *MYC*-NPLCs. Note that the overall survival of mice inoculated with *MYC*-NPLCs is significantly shorter than of control. Kaplan-Meier analysis was performed. ****$p<0.0001$ (Log-rank test).

A
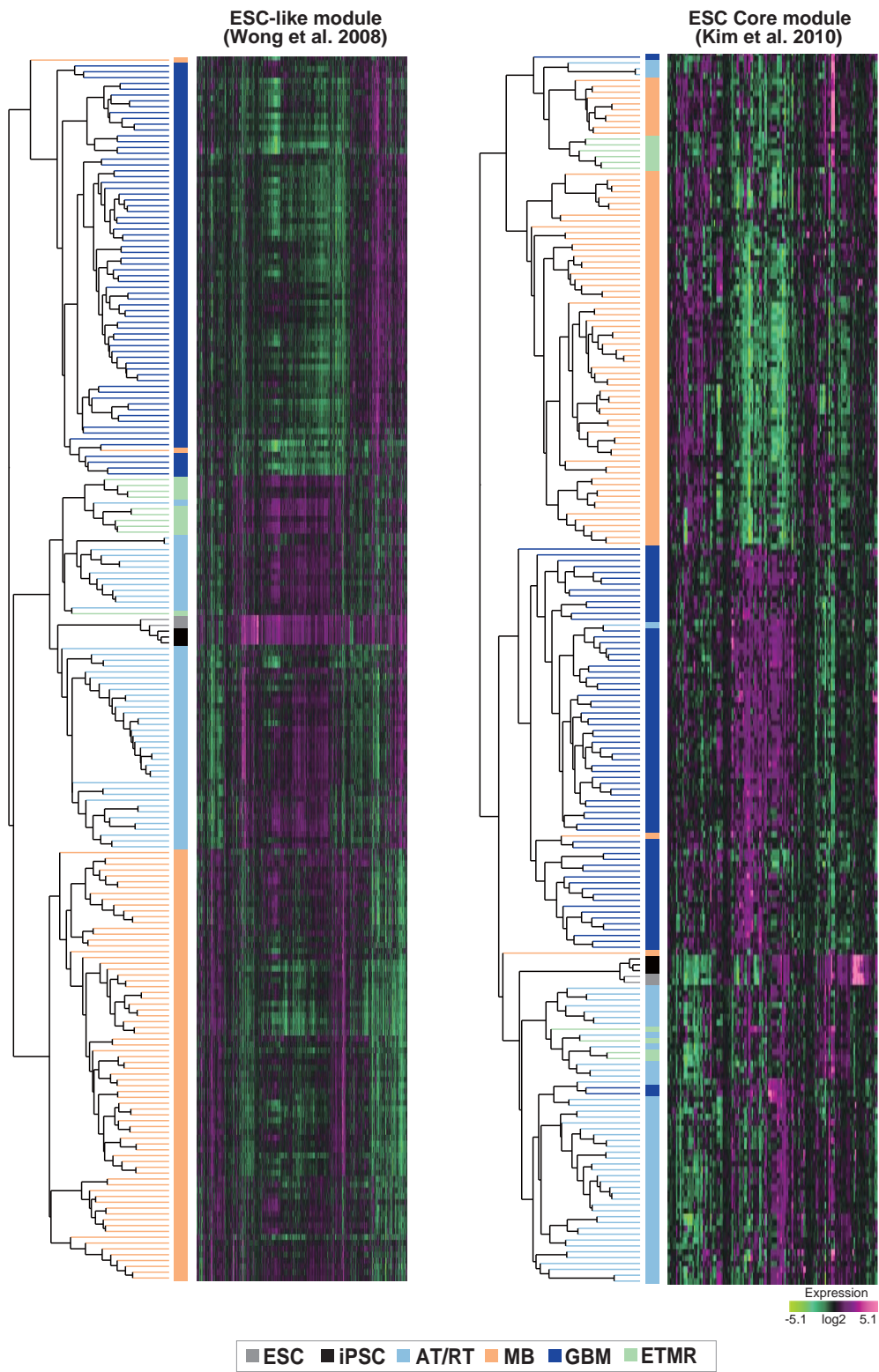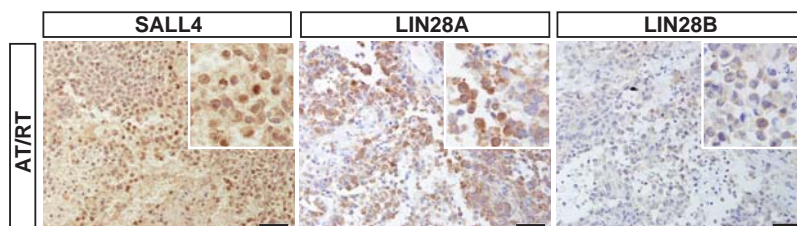
ESC-like module
(Wong et al. 2008)

ESC Core module
(Kim et al. 2010)

Expression

-5.1   log2   5.1

■ ESC ■ iPSC ■ AT/RT ■ MB ■ GBM ■ ETMR

B

SALL4   LIN28A   LIN28B

AT/RT

Figure S4: Human AT/RT specimens exhibit activation of the ESC-like gene expression signature, related to Figure 4

Figure S4: Human AT/RT specimens exhibit activation of the ESC-like gene expression signature, related to Figure 4

(A) Clustering analysis using microarray data revealed that both hESC-like module genes (left) and ESC Core module genes (right) are similarly expressed in AT/RT samples and ESCs/iPSCs. Note that some ETMRs were clustered with AT/RT samples and ESCs/iPSCs. Medulloblastoma (MB) and glioblastoma (GBM) samples are basically clustered separately from ESCs/iPSCs. The microarray data of hPSCs, AT/RTs, ETMRs, medulloblastomas and glioblastomas were obtained from GSE22392 (hESC/hiPSC), GSE73038 (ETMR), GSE70678 (AT/RT), GSE37418 (MB) and GSE53733 (GBM).

(B) Immunohistochemical analysis of SALL4, LIN28A and LIN28B in clinical AT/RT specimens. Scale bars, 50 μm.
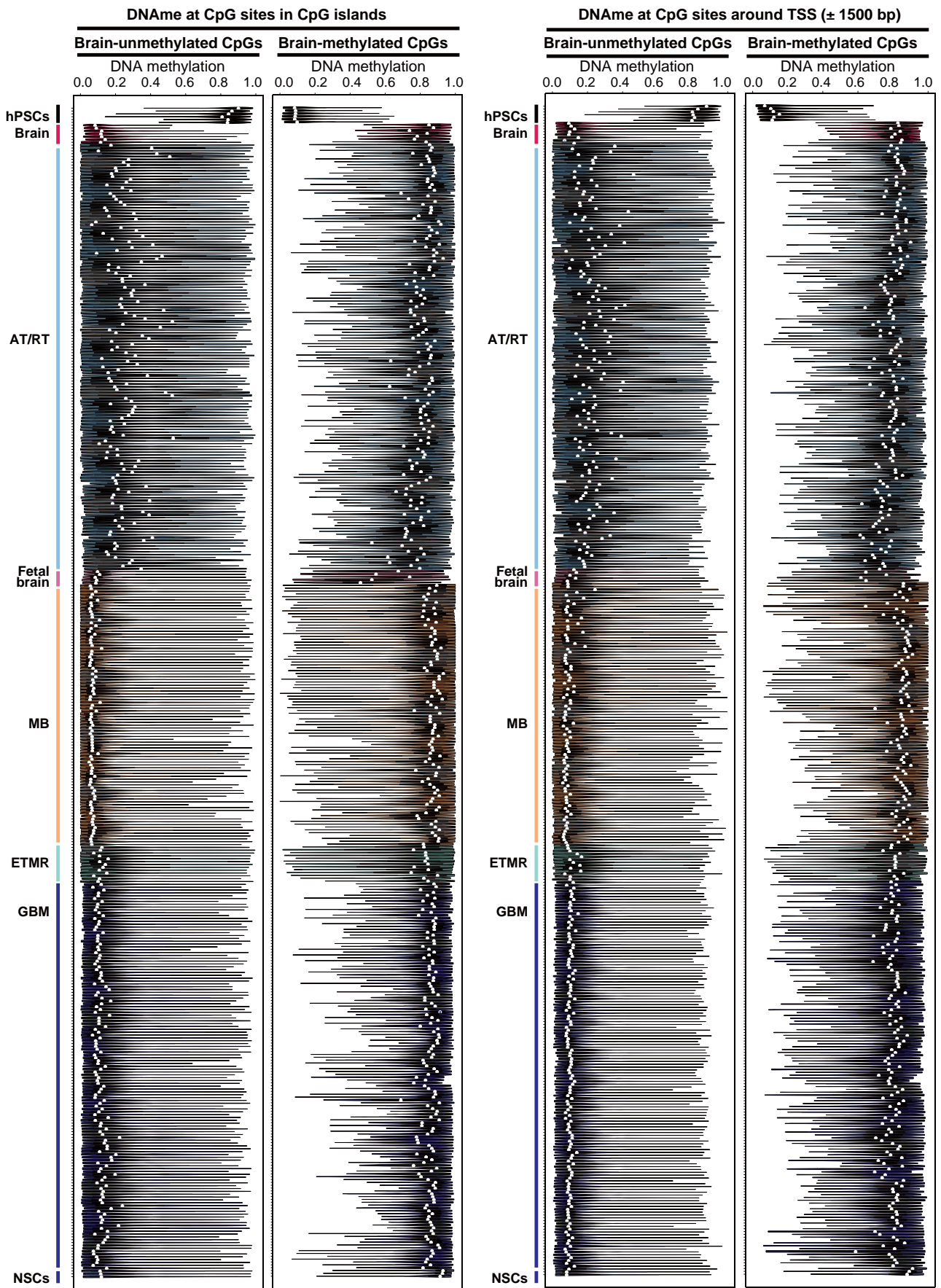
Figure S5: DNA methylation landscape in human AT/RT specimens, related to Figure 4

Figure S5: DNA methylation landscape in human AT/RT specimens, related to Figure 4

The DNA methylation landscape in AT/RTs analyzed using Infinium450K data. In this analysis, we first extracted differentially methylated CpG sites within CGIs (left) or around TSSs (right) between hPSCs and adult brains. hPSC-specific methylated CpG sites and adult brain-specific methylated CpG sites were analyzed for AT/RTs, ETMRs, medulloblastomas and glioblastomas as well as fetal brains and NSCs. AT/RTs harbor increased methylation at the PSC-specific methylated CpG sites, while adult brain-specific methylated CpG sites are less methylated in AT/RTs. Each dot indicates the median of DNA methylation at the analyzed CpG sites. Infinium450K data of hPSCs, normal brains, fetal brains, NSCs, AT/RTs, ETMRs, medulloblastomas and glioblasomas were obtained from GSE60821 (hPSC), GSE92462 (hPSC/NSC/normal brain/fetal brain), GSE36278 (normal brain/fetal brain/GBM), GSE73801 (ETMR), GSE75153 (MB) and GSE70460 (AT/RT).
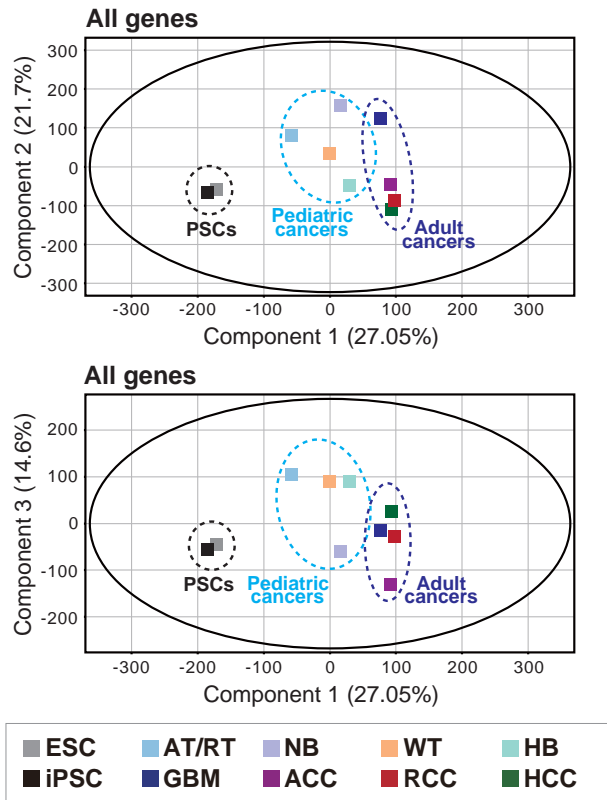
Figure S6: Pediatric cancers exhibit activation of the ESC-like gene expression signature, related to Figure 5

Figure S6: Pediatric cancers exhibit activation of the ESC-like gene expression signature, related to Figure 5

Principal component analysis of the global gene expression profiles in pediatric cancers and adult cancers. Pediatric cancers exhibit ESC-like gene expression patterns when compared to the corresponding adult cancers. AT/RT: atypical teratoid/rhabdoid tumor, NB: neuroblastoma, WT: Wilms tumor, HB: hepatoblastoma, GBM: glioblastoma, ACC: adrenocortical carcinoma, RCC: renal cell carcinoma, HCC: hepatocellular carcinoma. The same microarray data as Figure 5A were used.
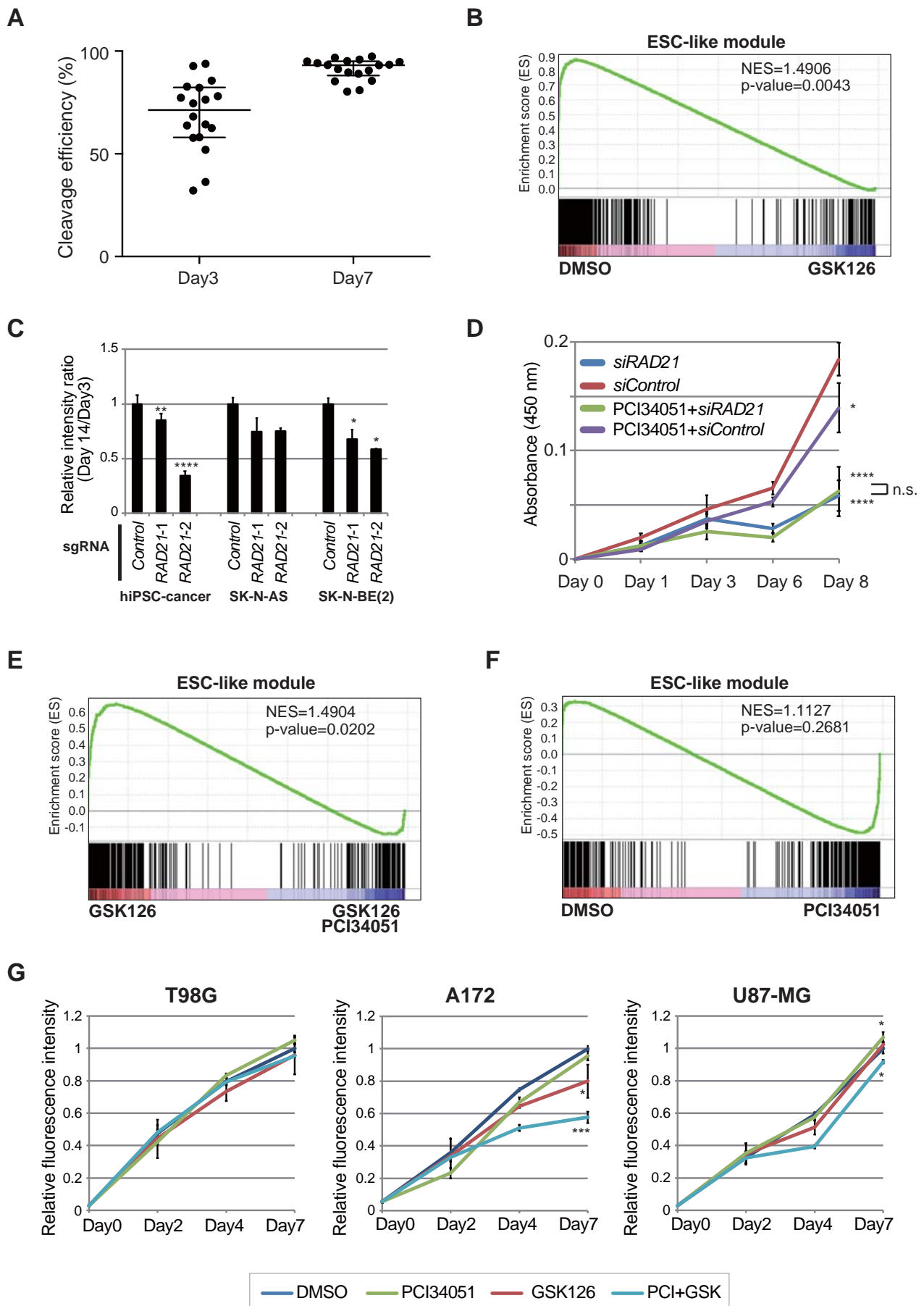
Figure S7: Genetic screening with CRISPR/Cas9 to develop a novel therapeutic strategy for AT/RT, related to Figure 6

Figure S7: Genetic screening with CRISPR/Cas9 to develop a novel therapeutic strategy for AT/RT, related to Figure 6

(A) The cleavage efficiency at Day 3 and Day 7 after lentiviral-mediated transduction of CRISPR/Cas9 together with sgRNAs in SK-N-BE(2) *in vitro*. sgRNAs for 18 randomly selected genes were transduced with CRISPR/Cas9, and the efficiency of non-homologous end joining was measured by TIDE software 3 and 7 days after the lentiviral transduction. Data are represented as the median with interquartile range.

(B) GSEA showing that EZH2 inhibition by GSK126 suppresses the ESC-like module in hiPSC-derived cancer cells.

(C) Growth ratios (Day 14/Day 3) of hiPSC-derived cancer cells, SK-N-AS and SK-N-BE(2) transduced with CRISPR/Cas9 with sgRNA for non-targeting control (NTC) or *RAD21*. Two independent sgRNAs for *RAD21* reduced the cell growth ratio compared to *NTC*. Data are presented as the mean of three biological replicates with standard deviation. The growth ratio of *NTC*-transduced cells was set to 1. *$p<0.05$, **$p<0.01$ and ****$p<0.0001$ (One-way ANOVA and Dunnett's multiple comparisons test).

(D) Cell viability of hiPSC-derived cancer cells treated with PCI34051 (10 μM) or the combination of PCI34051 (10 μM) and *siRAD21*. Note that the growth inhibitory effect of PCI34051 is not obvious in the presence of *siRAD21*. *$p<0.05$, ****$p<0.0001$ (One-way ANOVA and Dunnett's multiple comparisons test).

(E) GSEA revealed that suppression of the ESC-like module by GSK126 is further pronounced by the combination treatment of GSK126 and PCI34051.

(F) Sole inhibition of HDAC8 by PCI34051 does not suppress the ESC-like module in hiPSC-derived cancer cells.

(G) Cell viability of glioblastoma cell lines treated with DMSO, PCI34051 (10 μM), GSK126 (10 μM) or the combination of PCI34051 and GSK126 (10 μM each). *$p<0.05$, ***$p<0.001$ (One-way ANOVA and Dunnett's multiple comparisons test).

Table S1: List of 110 target genes and their oligos for sgRNA, related to Figure 6

Tagert genes associated with the maintenance of ESC identity	Oligos for sgRNA
hNTC	CACCCTGAAGGTGTCTGGCAGAGC
	AAACGCTCTGCCAGACACCTTCAG
LIN28B	CACCGCATCGACTGGAATATCCAAG
	AAACCTTGGATATTCCAGTCGATGC
TCF3	CACCCACGCCTGCGTCTCTCCCGA
	AAACTCGGGAGAGACGCAGGCGTG
MAP4K4	CACCTCAGGGTCGACATGTTAAAA
	AAACTTTTAACATGTCGACCCTGA
GLUL	CACCACGGAAGGGGTCCCGAAACA
	AAACTGTTTCGGGACCCCTTCCGT
ETV5	CACCCTGATCATAAAACCCGTCCA
	AAACTGGACGGGTTTTATGATCAG
RND2	CACCTGCGCCGAACTGACTCACGC
	AAACGCGTGAGTCAGTTCGGCGCA
MYCN	CACCCAGGCCGAACGCGTCCTCCT
	AAACAGGAGGACGCGTTCGGCCTG
JARID2	CACCCTTCATGCCAGTCGACCCCC
	AAACGGGGGTCGACTGGCATGAAG
NIPBL	CACCGCTTGTCCATAGCCTCAACC
	AAACGGTTGAGGCTATGGACAAGC
KLF9	CACCCACCGCAGCGCGGTTCGAAA
	AAACTTTCGAACCGCGCTGCGGTG
MYBL2	CACCATTCAGATGTGCCGGAGCAG
	AAACCTGCTCCGGCACATCTGAAT
IFITM1	CACCCAGAGCCGAATACCAGTAAC
	AAACGTTACTGGTATTCGGCTCTG
APOC1	CACCTGGAGACGTCTGGGGTCCCC
	AAACGGGGACCCCAGACGTCTCCA
UCK2	CACCGGACACGGTAGAAGCTATCC
	AAACGGATAGCTTCTACCGTGTCC
HLA-DPA1	CACCGGGCCTAGTCGGCATCATCG
	AAACCGATGATGCCGACTAGGCCC
EYA1	CACCGAAATTGTTTAAAGACCCGT
	AAACACGGGTCTTTAAACAATTTC
HTATIP2	CACCAGTCTTCCCGAAGCTTCGAC
	AAACGTCGAAGCTTCGGGAAGACT
PLA2G16	CACCATCATCGCTGCAAGCGTTGC
	AAACGCAACGCTTGCAGCGATGAT
HNRNPUL1	CACCCCGTGTATGCTTCGAGATGA
	AAACTCATCTCGAAGCATACACGG
SLC15A1	CACCCGCCATCTACCATACGTTTG
	AAACCAAACGTATGGTAGATGGCG
ENAH	CACCCCTGTCTAGCATCTCGCCAC
	AAACGTGGCGAGATGCTAGACAGG
MYBPH	CACCCCGTCAGACCTACATCCGCC
	AAACGGCGGATGTAGGTCTGACGG
IGFBP2	CACCGCTCCTTCATACCCGACTTG
	AAACCAAGTCGGGTATGAAGGAGC
SOX2	CACCATTATAAATACCGGCCCCGG
	AAACCCGGGGCCGGTATTTATAAT
NANOG	CACCTTCTTACCGTCTCCGTGTG
	AAACCACACGGAGACTGGTAAGAA
POU5F1	CACCACTTGCAGGTGGTCCGAGTG
	AAACCACTCGGACCACCTGCAAGT
EYA2	CACCGCTTGTCGTACTCCACTTTG
	AAACCAAAGTGGAGTACGACAAGC
SETD8	CACCGACGGAGCGCCATGAAGTCCG
	AAACCGGACTTCATGGCGCTCCGTC
CENPE	CACCGTGGCCGTCTGCGTGCGAGTG
	AAACCACTCGCACGCAGACGGCCAC
CHAF1A	CACCGCTCGGGCCACTCGTCAGCTC
	AAACGAGCTGACGAGTGGCCCGAGC
INCENP	CACCGAGGCCGAGCGCATGTTCACC
	AAACGGTGAACATGCGCTCGGCCTC
MSH6	CACCGAGGAAGCTCACCTTCGACG
	AAACCGTCGAAGGTGAGCTTCCTC
FN1	CACCGACCTACCTAGGCAATGCGT
	AAACACGCATTGCCTAGGTAGGTC
ANP32A	CACCGTAGCCCTCAGCATCCGAGTC
	AAACGACTCGGATGCTGAGGGCTAC
NFKBIA	CACCGCCTGAGCTCCGAGACTTTCG
	AAACCGAAAGTCTCGGAGCTCAGGC
GJA1	CACCGTCAGCGCACCACTGGTCGCA

GJA1	AAACTGCGACCAGTGGTGCGCTGAC
CRMP1	CACCGCTCCCGGAGAGCGCGACGAG
	AAACCTCGTCGCGCTCTCCGGGAGC
DST	CACCGTCACTCCAGCTTATACACC
	AAACGGTGTATAAGCTGGAGTGAC
CAMK2N1	CACCGACCAACAACTTCTTCGGCGC
	AAACGCGCCGAAGAAGTTGTTGGTC
IFITM2	CACCGCTCATCATCATCCCAGTGT
	AAACACACTGGGATGATGATGAGC
SIX2	CACCGCGGGAATTTGCGGCGCACG
	AAACCGTGCGCCGCAAATTCCCGC
PAX8	CACCGATGCGCTGGCGGACCACTTC
	AAACGAAGTGGTCCGCCAGCGCATC
PHOX2B	CACCGAGGTCCTTACCTGCGGCGTA
	AAACTACGCCGCAGGTAAGGACCTC
IGF2	CACCGCATAGACGCGAGTTCGGTCT
	AAACAGACCGAACTCGCGTCTATGC
PAX2	CACCGGCCCCTACCCGACGTGGTG
	AAACCACCACGTCGGGTAGGGGCC
LMO1	CACCGTGTGCCGACGCGACTACCTG
	AAACCAGGTAGTCGCGTCGGCACAC
CRABP2	CACCGCACAACGTCATCCGCCGTCA
	AAACTGACGGCGGATGACGTTGTGC
C1QB	CACCGAACAATTATGAGCCCCGCAG
	AAACCTGCGGGGGCTCATAATTGTTC
PRAME	CACCGTCTACGCAGATTAATCATC
	AAACGATGATTAATCTGCGTAGAC
RGS4	CACCGACTTACATTCATGACTAATC
	AAACGATTAGTCATGAATGTAAGTC
GPR64	CACCGCATTTGTCTTCATGTCGTTC
	AAACGAACGACATGAAGACAAATGC
RGS5	CACCGATGTAGAACCTCGCTGGACG
	AAACCGTCCAGCGAGGTTCTACATC
MYC	CACCGAACGTTGAGGGGCATCGTCG
	AAACCGACGATGCCCCTCAACGTTC
HMGA1	CACCGGGCATCTCGCAGGAGTCCT
	AAACAGGACTCCTGCGAGATGCCC
HMGA2	CACCGTGGCGCCCCCTAGTCCTCTT
	AAACAAGAGGACTAGGGGGCGCCAC
EZH2_1	CACCGGTCCCAATTAACCTAGCAA
	AAACTTGCTAGGTTAATTGGGACC
EZH2_2	CACCGTGGTGGATGCAACCCGCAA
	AAACTTGCGGGTTGCATCCACCAC
ARID1A	CACCGCAGCAGAACTCTCACGACCA
	AAACTGGTCGTGAGAGTTCTGCTGC
ARID4A	CACCGATGCTAGTTGGTATACCGT
	AAACACGGTATACCAACTAGCATC
CBX3	CACCGAGAGCCTGAAGAATTTGTCG
	AAACCGACAAATTCTTCAGGCTCTC
CDK8	CACCGAGGGCTGCAAAGTTGGCCG
	AAACCGGCCAACTTTGCAGCCCTC
CHD7	CACCGTGGGCAGCTATATGGCACGT
	AAACACGTGCCATATAGCTGCCCAC
EDF1	CACCGACATTCTATTACCAAGAACA
	AAACTGTTCTTGGTAATAGAATGTC
FUBP1	CACCGTGATTGTAACAGGAACGGGC
	AAACGCCCGTTCCTGTTACAATCAC
H1FX	CACCGCTGGCCAAGATCTACACCG
	AAACCGGTGTAGATCTTGGCCAGC
H2AFZ	CACCGACAACTACTGACCTGCAAGC
	AAACGCTTGCAGGTCAGTAGTTGTC
MAX	CACCGTATTCCAGGAAGAGCAACCG
	AAACCGGTTGCTCTTCCTGGAATAC
MGA	CACCGACTGGAATCAACAACAATCG
	AAACCGATTGTTGTTGATTCCAGTC
RIF1	CACCGACATGACACGAATTGCCCTG
	AAACCAGGGCAATTCGTGTCATGTC
SETDB1	CACCGCCTTACCTGAATCAATACTG
	AAACCAGTATTGATTCAGGTAAGGC
SMAD2	CACCGCTAAATGTGTTACCATACCA
	AAACTGGTATGGTAACACATTTAGC
SMAD3	CACCGAGAAGCGCTCCGAATTGGAG
	AAACCTCCAATTCGGAGCGCTTCTC
SMARCA4	CACCGGGCGTACGAGTTTGACAAG
	AAACCTTGTCAAACTCGTACGCCC
SMARCC1	CACCGTGTTAAAGGAGGAACTGTAG
	AAACCTACAGTTCCTCCTTTAACAC

STAT3	CACCGACGCCGGTCTTGATGACGAG
	AAACCTCGTCATCAAGACCGGCGTC
SUPT16H	CACCGAATGTCAGTACCTTGATTG
	AAACCAATCAAGGTACTGACATTC
TIMP2	CACCGTTTATGGCAACCCTATCAAG
	AAACCTTGATAGGGTTGCCATAAAC
ZNF136	CACCGAAAGATCACTACAAACACCG
	AAACCGGTGTTTGTAGTGATCTTTC
ZNF43	CACCGATGAGTGTAAGGTGCACAG
	AAACCTGTGCACCTTACACTCATC
MED1	CACCGCCAGTAATAGTACTCTCTCG
	AAACCGAGAGAGTACTATTACTGGC
RAD21_1	CACCGTCTGTTCAGACTCTAATAGG
	AAACCCTATTAGAGTCTGAACAGAC
RAD21_2	CACCGTGTAATTTAGAGAGCAGCG
	AAACCGCTGCTCTCTAAATTACAC
CBX1	CACCGGCCGACTCACCATTTCATC
	AAACGATGAAATGGTGAGTCGGCC
CHD1	CACCGTTAATTCGCCTAAGAGAACG
	AAACCGTTCTCTTAGGCGAATTAAC
YY1	CACCGTGAACAAACGCTGGTCACCG
	AAACCGGTGACCAGCGTTTGTTCAC
CDC5L	CACCGAATTGCACGTCAAACTGCCG
	AAACCGGCAGTTTGACGTGCAATTC
DDX47	CACCGTCCTCTATTGGAGTGCAGAG
	AAACCTCTGCACTCCAATAGAGGAC
DHX15	CACCGTGGGTCTGGTAAAACAACAC
	AAACGTGTTGTTTTACCAGACCCAC
LUC7L3	CACCGTAGAACGTAGGATCAGACG
	AAACCGTCTGATCCTACGTTCTAC
MCM6	CACCGCTGCGGGGGATACTCCCTCG
	AAACCGAGGGAGTATCCCCCGCAGC
MCM7	CACCGAAGCCCAACTACTTACTGCG
	AAACCGCAGTAAGTAGTTGGGCTTC
RTF1	CACCGTGTCCGAGTCGATCACGACG
	AAACCGTCGTGATCGACTCGGACAC
SMC1A	CACCGATTGCCACAAGCATACTGCA
	AAACTGCAGTATGCTTGTGGCAATC
SMC4	CACCGCATTGATGAAAAATACGACG
	AAACCGTCGTATTTTTCATCAATGC
SNRPD2	CACCGACCCAGCACTCACCTATCGA
	AAACTCGATAGGTGAGTGCTGGGTC
SSRP1	CACCGACCACGAGCAAAGTTGACAA
	AAACTTGTCAACTTTGCTCGTGGTC
THAP11	CACCGGAGAAGCACCCACTGACGC
	AAACGCGTCAGTGGGTGCTTCTCC
TPR	CACCGACCTGGGATGAAACTAACTG
	AAACCAGTTAGTTTCATCCCAGGTC
WDR82	CACCGTTTCAGCCCCAACGGCGAGA
	AAACTCTCGCCGTTGGGGCTGAAAC
SUV39H2	CACCGAATCTAAACAATTATGAGG
	AAACCCTCATAATTGTTTAGATTC
TRIM28	CACCGCTTCCCAGGCAGTACCACTG
	AAACCAGTGGTACTGCCTGGGAAGC
EIF4A3	CACCGCCGCATCTTGGTGAAACGGT
	AAACACCGTTTCACCAAGATGCGGC
EED	CACCGTTGTGAATGACATTCATACA
	AAACTGTATGAATGTCATTCACAAC
SOX11	CACCGCGACCCAGACTGGTGCAAGA
	AAACTCTTGCACCAGTCTGGGTCGC
FOXM1	CACCGCCTGGTCCAATGTCAAGTAG
	AAACCTACTTGACATTGGACCAGGC
E2F7	CACCGCAGAGGGCACATACACTAG
	AAACCTAGTGTATGTGCCCTCTGC
ETV1	CACCGAGTGTATGAACACAACACCA
	AAACTGGTGTTGTGTTCATACACTC
TCF4	CACCGACTACAATAGGGACTCGCC
	AAACGGCGAGTCCCTATTGTAGTC
BCL11A	CACCGTGAAGGGATACCAACCCGCG
	AAACCGCGGGTTGGTATCCCTTCAC
WHSC1	CACCGCACCAGCTCACGTTGACGT
	AAACACGTCAACGTGAGCTGGTGC
KDM5B	CACCGACACCTTCGCCTAGTCACAC
	AAACGTGTGACTAGGCGAAGGTGTC
MTA1	CACCGTGTGGAGAGTATCCATGGCG
	AAACCGCCATGGATACTCTCCACAC

Table S2: References for picking out 110 target genes, related to Figure 6

First author	Reference
Doench JG	Nat Biotechnol. 2016, 34(2):184-191
Kim J	Cell. 2010, 143(2):313-24
Takahashi K	Cell. 2016, 126(4):663-76
Veschi V	Cancer Cell. 2017, 31(1):50-63
Zhang K	Clin Cancer Res. 2014, 20(5):1179-89
Kaur H	J Neuropathol Exp Neurol. 2015, 74(2):177-85
Alimova I	Neuro Oncol. 2013, 15(2):149-60
Fazzio TG	Cell. 2008, 134(1):162-74
Young RA	Cell. 2011, 144(6):940-54
Urbach A	Genes Dev. 2014, 1;28(9):971-82
Molenaar JJ	Nat Genet. 2012, 44(11):1199-206
Chia NY	Nature. 2010, 468(7321):316-20
Hu G	Genes Dev. 2009, 23(7):837-48
Abujarour R	Stem Cells. 2010, 28(9):1487-97
Weingart MF	Oncotarget. 2015, 6(5):3165-77
Sanjana NE	Nat Methods. 2014, 11(8):783-4
Collinson A	Cell Rep. 2016, 17(10):2700-14

Table S3: Results of genetic screening with lentiviral CRISPR/Cas9 system, related to Figure 6

hiPSC-derived cancer cells

Rank	Gene Name	Relative growth ratio compared to contorol	SD
1	FN1	0.473713218	0.064243312
2	IFITM2	0.601700671	0.079338947
3	PRAME	0.624056884	0.104260527
4	SETD8	0.630024573	0.032886971
5	SNRPD2	0.684795705	0.067667121
6	SMC4	0.699734173	0.130264191
7	C1QB	0.721125506	0.027325322
8	TCF3	0.737204194	0.017689598
9	EZH2	0.743813879	0.031221687
10	MYCN	0.74718664	0.049478903
11	EIF4A3	0.764182888	0.049226373
12	IFITM1	0.777677083	0.011620789
13	MAP4K4	0.77853271	0.038224403
14	GLUL	0.778803996	0.071004748
15	JARID2	0.790290675	0.039910139
16	ETV5	0.803919269	0.052786473
17	MYBL2	0.812490684	0.008053099
18	UCK2	0.832108769	0.055738043
19	APOC1	0.835838286	0.035569568
20	BCL11A	0.836508025	0.051817538
21	KLF9	0.847305588	0.054453079
22	RAD21	0.851195014	0.060688001
23	HNRNPUL1	0.859588338	0.008848117
24	HLA-DPA1	0.862452736	0.065881531
25	CAMK2N1	0.865428957	0.051593928
26	EYA2	0.866678259	0.047308828
27	DHX15	0.878604134	0.158983685
28	MYBPH	0.888863478	0.02228249
29	PLA2G16	0.89124223	0.028606255
30	SLC15A1	0.893447815	0.044758462
31	NIPBL	0.898832048	0.011430032
32	TCF4	0.913598879	0.003228589
33	POU5F1	0.913767301	0.03421047
34	CRABP2	0.916729641	0.088531672
35	CENPE	0.917613413	0.004209638
36	FOXM1	0.922542662	0.040502371
37	SOX11	0.923229395	0.009800014
38	SMC1A	0.923714236	0.063992056
39	RND2	0.924167105	0.09175922
40	THAP11	0.925627053	0.01227535
41	RGS5	0.934344192	0.034692423
42	INCENP	0.934491407	0.086727669
43	TPR	0.937488377	0.030652308
44	SOX2	0.939579377	0.015416376
45	NANOG	0.947840479	0.039180125
46	HMGA1	0.956009234	0.016494905
47	ENAH	0.958993037	0.02282592
48	MYC	0.96444836	0.053700882
49	SUV39H2	0.964944735	0.038070788
50	LUC7L3	0.967701384	0.031203097
51	EYA1	0.973212321	0.037066058
52	SSRP1	0.984356995	0.051497718
53	E2F7	0.987737046	0.039588074
54	RTF1	0.992455009	0.008702249
55	PAX2	0.99305148	0.018531997
56	ANP32A	0.996628905	0.002767853
57	LIN28B	0.997706827	0.030467343
58	hNTC	1	0.03228208
59	DST	1.001685756	0.044369644
60	GJA1	1.002986873	0.048744042
61	MCM7	1.009580956	0.038391653
62	PAX8	1.011599431	0.054704041
63	TRIM28	1.015925545	0.052812528
64	IGF2	1.018768979	0.048452086
65	CHAF1A	1.019569065	0.053726003
66	DDX47	1.019614249	0.024087719
67	IGFBP2	1.022850516	0.130231852
68	MCM6	1.025198368	0.020890819
69	ZNF43	1.026718922	0.014895802
70	LMO1	1.027048617	0.022904104
71	CBX1	1.028057096	0.092297571
72	MTA1	1.030018251	0.037264447
73	GPR64	1.030509761	0.030482975
74	CRMP1	1.032984939	0.069514021
75	CBX3	1.03483747	0.02459842
76	SMAD3	1.035063859	0.027596984
77	RGS4	1.035576599	0.064922005
78	SUPT16H	1.039592187	0.011919653
79	PHOX2B	1.047577482	0.014977001
80	MAX	1.049063812	0.01553368
81	CDK8	1.0503878	0.034368434
82	SMARCA4	1.050994915	0.007792492
83	SIX2	1.055854942	0.040821165
84	ARID4A	1.057425882	0.011797434
85	NFKBIA	1.057981618	0.097235452
86	H2AFZ	1.060835877	0.031733782
87	MGA	1.061182685	0.033528636
88	SMARCC1	1.063659763	0.018690698
89	EED	1.065043176	0.058118364
90	TIMP2	1.066063103	0.032476205
91	SMAD2	1.070264506	0.022879782
92	H1FX	1.072841563	0.053793748
93	CHD7	1.076817451	0.037121991
94	YY1	1.079569319	0.039026623
95	FUBP1	1.080830931	0.022007283
96	MSH6	1.081696089	0.019827689
97	MED1	1.097654637	0.022986743
98	CDC5L	1.109372871	0.050598035
99	EDF1	1.110216144	0.051350721
100	ZNF136	1.117405554	0.028086986
101	ARID1A	1.119694063	0.031637066
102	SETDB1	1.120265621	0.02488206
103	RIF1	1.126121047	0.010969745
104	WDR82	1.127288957	0.046816292
105	HMGA2	1.141975854	0.046444506
106	WHSC1	1.148405364	0.020486602
107	CHD1	1.150064716	0.035342853
108	STAT3	1.162237302	0.008364431
109	ETV1	1.219780016	0.128501961
110	HTATIP2	1.24005642	0.026421063
111	KDM5B	1.271766098	0.278748792

SK-N-AS

Rank	Gene Name	Relative growth ratio compared to contorol	SD
1	EIF4A3	0.169565387	0.009805383
2	INCENP	0.527737752	0.013365749
3	DDX47	0.644558025	0.007870972
4	MCM7	0.66923558	0.016852987
5	WDR82	0.675463706	0.03716815
6	LUC7L3	0.683279843	0.014687562
7	PHOX2B	0.68995379	0.008922695
8	CDC5L	0.693336429	0.005673633
9	SNRPD2	0.696611714	0.034632283
10	CHAF1A	0.702607795	0.055870782
11	SSRP1	0.716823563	0.036719143
12	EYA2	0.732362823	0.07205275
13	TPR	0.737355215	0.028882318
14	RAD21	0.747631663	0.121261803
15	DHX15	0.755507112	0.075774477
16	C1QB	0.765545571	0.037311765
17	MCM6	0.770667755	0.034568063
18	DST	0.779968272	0.046493809
19	NANOG	0.7852302	0.124220033
20	RTF1	0.788666151	0.018072722
21	SMC1A	0.804984617	0.073380992
22	MYC	0.80943862	0.012560515
23	NFKBIA	0.814613849	0.072556011
24	IFITM2	0.814791199	0.022504999
25	SOX2	0.820547874	0.050932206
26	MYBL2	0.823530108	0.044051622
27	HMGA1	0.823551052	0.019301681
28	POU5F1	0.834678327	0.07933968
29	CRABP2	0.837321721	0.009594555
30	THAP11	0.840812994	0.021677715
31	TRIM28	0.840892971	0.097667164
32	SUPT16H	0.84338783	0.041601944
33	EED	0.845130685	0.040163579
34	LIN28B	0.85108255	0.135128323
35	CAMK2N1	0.874436434	0.021487793
36	CENPE	0.875624545	0.054640938
37	SETD8	0.877680583	0.057412923
38	YY1	0.879327529	0.033394962
39	CHD1	0.89024884	0.047361739
40	TIMP2	0.910001826	0.019170634
41	SUV39H2	0.911920696	0.068101775
42	IGF2	0.912607631	0.027133803
43	IGFBP2	0.925028892	0.093294768
44	NIPBL	0.926839353	0.069389496
45	EDF1	0.940227719	0.087414044
46	CHD7	0.958289333	0.031230682
47	PAX2	0.961687727	0.026204026
48	SMARCA4	0.964495493	0.009502328
49	FUBP1	0.964785045	0.029821963
50	SMC4	0.969079091	0.069771416
51	ARID1A	0.969262322	0.015790648
52	MAX	0.970574745	0.022727964
53	LMO1	0.973947123	0.030277472
54	RIF1	0.978593715	0.074609039
55	SMAD3	0.989914087	0.019388857
56	PAX8	0.992282333	0.059223962
57	UCK2	0.997291056	0.037441333
58	SMARCC1	0.998004712	0.029855718
59	PRAME	0.999415342	0.045707195
60	hNTC	1	0.069772848
61	SETD81	1.003438736	0.042353556
62	EZH2	1.004972622	0.031265839
63	CRMP1	1.008382645	0.024593584
64	CBX3	1.009179469	0.046725171
65	ANP32A	1.010391678	0.033761899
66	SIX2	1.010971216	0.033826736
67	RGS5	1.015686882	0.012107737
68	SMAD2	1.018613596	0.057613405
69	FN1	1.019482023	0.043113878
70	MGA	1.032093197	0.05340931
71	CDK8	1.033383322	0.030819523
72	GJA1	1.035622325	0.065187863
73	MED1	1.052961765	0.023867936
74	ZNF43	1.056187822	0.057608862
75	CBX1	1.060030611	0.089459156
76	PLA2G16	1.060361987	0.016154541
77	RGS4	1.060911813	0.097107471
78	MSH6_2	1.061137934	0.040835141
79	ARID4A	1.065230337	0.028242087
80	H1FX	1.074440737	0.035540789
81	TCF3	1.085152051	0.154322066
82	H2AFZ	1.088555744	0.025901837
83	ZNF136	1.098326367	0.032473232
84	GPR64	1.101578418	0.00571393
85	HMGA2	1.10477116	0.046863576
86	STAT3	1.106066933	0.03976361
87	FOXM1	1.182992117	0.053552744
88	APOC1	1.201390586	0.061976176
89	HNRNPUL1	1.211376924	0.03130036
90	IFITM1	1.222479321	0.16351548
91	SOX11	1.265689384	0.049950114
92	BCL11A	1.269249166	0.072630455
93	TCF4	1.290443945	0.013844829
94	SLC15A1	1.329457088	0.045047255
95	MAP4K4	1.345945572	0.121853915
96	WHSC1	1.358066892	0.021668405
97	JARID2	1.392056741	0.072347197
98	MTA1	1.411135363	0.130293187
99	MYCN	1.441390666	0.046718904
100	GLUL	1.442074071	0.083110734
101	E2F7	1.45236403	0.058137901
102	ENAH	1.512990909	0.041715052
103	KDM5B	1.518139597	0.051182514
104	MYBPH	1.579735763	0.054012904
105	ETV5	1.620459123	0.108366003
106	HLA-DPA1	1.744922707	0.158093226
107	ETV1	1.755095567	0.049681282
108	RND2	1.80329171	0.163430477
109	HTATIP2	2.087640063	0.186598968
110	KLF9	2.333761653	0.174994017
111	EYA1	2.53060758	0.224590751

SK-N-BE(2)

Rank	Gene Name	Relative growth ratio compared to contorol	SD
1	MYCN	0.30760042	0.006681813
2	SUPT16H	0.348697118	0.04708912
3	EIF4A3	0.41083802	0.025312479
4	SETDB1	0.525616952	0.058120662
5	DDX47	0.673008303	0.004742421
6	RAD21	0.67591018	0.089722782
7	TIMP2	0.698883957	0.047643183
8	CDC5L	0.755521981	0.034751615
9	LUC7L3	0.768067499	0.081317428
10	EZH2	0.797878906	0.091969876
11	SMC1A	0.800888766	0.043694774
12	MCM6	0.807855081	0.044683803
13	YY1	0.819126043	0.022523618
14	SNRPD2	0.829977136	0.042859664
15	RTF1	0.83448445	0.084633429
16	THAP11	0.839345055	0.045945844
17	FUBP1	0.841668009	0.044114001
18	EED	0.850379696	0.060952255
19	DHX15	0.859217002	0.051654761
20	SETD8	0.872510077	0.05216399
21	TPR	0.881572011	0.014919359
22	MCM7	0.891909855	0.095691889
23	WDR82	0.90256298	0.020174874
24	MYBL2	0.914257653	0.046015055
25	SMC4	0.920549927	0.071579455
26	CRMP1	0.931479687	0.032254534
27	EDF1	0.932464322	0.091600732
28	LIN28B	0.934563892	0.020976851
29	ANP32A	0.940729803	0.032435559
30	MGA	0.94145195	0.123114295
31	TRIM28	0.950994798	0.023134902
32	HMGA1	0.966226807	0.104183429
33	SMAD3	0.97201216	0.182632686
34	CHD1	0.975064385	0.10105166
35	ZNF136	0.998032135	0.349278622
36	hNTC	1	0.074491065
37	GJA1	1.000052694	0.022941246
38	CENPE	1.010773235	0.017901575
39	PAX8	1.012416037	0.045168022
40	SMAD2	1.014108917	0.13944452
41	PHOX2B	1.015792563	0.025960211
42	INCENP	1.018297675	0.033830618
43	MAX	1.019900888	0.031910642
44	IGF2	1.038329382	0.094353461
45	SIX2	1.043797056	0.029718442
46	UCK2	1.048853457	0.051709103
47	CBX3	1.049024649	0.125173108
48	SSRP1	1.056972145	0.057920072
49	CHD7	1.072602867	0.136798827
50	SUV39H2	1.08837556	0.034538565
51	PAX2	1.090052358	0.013647572
52	SOX2	1.095289468	0.087804425
53	MSH6_2	1.098389799	0.047546164
54	RIF1	1.103591236	0.170667944
55	CDK8	1.109201741	0.087316483
56	HMGA2	1.121950403	0.132672122
57	RGS5	1.124248181	0.038604092
58	CBX1	1.128212499	0.05438669
59	FOXM1	1.144101657	0.024373021
60	TCF4	1.147873706	0.044177141
61	STAT3	1.151953475	0.183347228
62	BCL11A	1.153907184	0.045437751
63	LMO1	1.154653788	0.091792006
64	MTA1	1.155682319	0.071549524
65	EYA2	1.161538966	0.044899249
66	CHAF1A	1.182820702	0.023513641
67	GPR64	1.189148551	0.01187839
68	IGFBP2	1.200468476	0.067726241
69	POU5F1	1.207771613	0.122413129
70	ZNF43	1.208109021	0.387610777
71	MYC	1.211936704	0.064926536
72	NIPBL	1.225542162	0.024078461
73	DST	1.227856041	0.0883124
74	H2AFZ	1.235172636	0.122688269
75	E2F7	1.240871988	0.082899533
76	C1QB	1.250473319	0.09249421
77	NANOG	1.259377244	0.114304222
78	NFKBIA	1.260062699	0.045858298
79	CAMK2N1	1.268463505	0.021814396
80	SLC15A1	1.278713428	0.061889134
81	MED1	1.303813441	0.022923171
82	ARID1A	1.305570971	0.221027127
83	WHSC1	1.307680009	0.036630042
84	KLF9	1.314040001	0.050674121
85	H1FX	1.316887364	0.059939772
86	SMARCA4	1.329257585	0.557852373
87	SOX11	1.331771385	0.107782256
88	APOC1	1.335807366	0.065179055
89	GLUL	1.350770148	0.090388672
90	SMARCC1	1.355346679	0.433879977
91	IFITM2	1.361292041	0.029815603
92	CRABP2	1.38470777	0.231038172
93	HNRNPUL1	1.399116379	0.070087878
94	MYBPH	1.400569057	0.149347363
95	PLA2G16	1.412178723	0.069008558
96	ARID4A	1.415399709	0.059169761
97	RGS4	1.424994737	0.070703087
98	HLA-DPA1	1.425461723	0.068160783
99	KDM5B	1.428454545	0.054646645
100	ENAH	1.49774191	0.134021268
101	FN1	1.507854005	0.055364462
102	IFITM1	1.593387131	0.021176676
103	JARID2	1.617929905	0.093778484
104	RND2	1.623044227	0.087759961
105	ETV5	1.652729228	0.418006596
106	EYA1	1.792898283	0.207899864
107	ETV1	1.823783525	0.054252776
108	TCF3	1.850068304	0.056942047
109	MAP4K4	1.890700021	0.087464659
110	PRAME	1.930211441	0.27164313
111	HTATIP2	1.965732453	0.164307093

Table S4: Primer list, related to STAR Methods

Genes	Forward	Reverse
Quantitative PCR		
GAPDH	ATGGGGAAGGTGAAGGTCG	GGGGTCATTGATGGCAACAATA
NANOG	TGAGATGCCTCACACGGAGA	GTTTGCCTTTGGGACTGGTG
OCT4	CGTGAAGCTGGAGAAGGAGAAGCTG	CAAGGGCCGCAGCTTACACATGTTC
NESTIN	CAGCTGGCGCACCTCAAGATG	AGGGAAGTTGGGCTCAGGACTGG
NCAM1	GAGGAGGAGAGGACCCCAAA	CTGGCACTCTGGCTTTGCTT
PAX6	CAGCTCGGTGGTGTCTTTGTCA	CTGCGCCCATCTGTTGCTTTTC
SALL4	CAACATTTGTGGGCGAGCTT	GCGGGCTGAGTTATTGTTCG
LIN28B	GTGGGAGCCCCTGTTTAGGA	CATGATGATCAAGGCCACCA
SOX2	CGGAAAACCAAGACGCTCA	GCCGTTCATGTAGGTCTGCG
c-MYC	CCTGGTGCTCCATGAGGAGA	GCCTGCCTCTTTTCCACAGA
MAP2	AGAGGGTGCCTTTGGAGAGC	TGCAGACACCTCCTCTGCTG
TUJ1	GGCCAAGGGTCACTACACG	GCAGTCGCAGTTTTCACACTC
CDKN2A	GTGGACCTGGCTGAGGAG	CTTTCAATCGGGGATGTCTG
E2F1	TCCAAGAACCACATCCAGTG	CTGGGTCAACCCCTCAAG
CCND1	GAAGATCGTCGCCACCTG	GACCTCCTCCTCGCACTTCT
GFAP	CGTGCAGACCTTCTCCAACC	GCATCTCCACGGTCTTCACC
Quantitative PCR for transduction of *pMxs-OCT4, SOX2, KLF4* and c-*MYC*		
c-MYC	ATACATCCTGTCCGTCCAAGCAGA	GACATGGCCTGCCCGGTTATTATT
SOX2	TTCACATGTCCCAGCACTACCAGA	GACATGGCCTGCCCGGTTATTATT
KLF4	CCACCTCGCCTTACACATGAAGA	GACATGGCCTGCCCGGTTATTATT
OCT4	GCTCTCCCATGCATTCAAACTGA	CTTACGCGAAATACGGGCAGACA
Direct sequencing		
SMARCB1	CTCGCTGACTGTTGCTTCCA	ACGGGACTGTTCCCACGTAA
TP53	TGTGCAGCTGTGGGTTGATT	CGCAAATTTCCTTCCACTCG